

SENSOR AND SIMULATION NOTES

Note 325

April 1990

GIGAHERTZ ANALYSIS OF THE ELLIPTICUS ANTENNA

Nicolas H. Younan

Bobby L. Cox

Department of Electrical and Computer Engineering

Mississippi State University

Mississippi State, MS 39762

Abstract

Efficient numerical solution techniques have been developed and used to examine the electromagnetic fields that can be developed in the working volume of the CW Ellipticus antenna operated at frequencies from 100 KHz to 1 GHz. An elliptically tapered transition section is designed and tested to obtain the desired illumination pattern in the working volume. A parametric study is performed to ascertain the performance of the Ellipticus antenna for frequencies up to 1 GHz.

CLEARED FOR PUBLIC RELEASE
PL/PA 25 Mar 91
PL 91-0059

CONTENTS

I	Introduction	3
	1.1 Background	3
	1.2 Scope of the Investigations	3
II	Description of the Ellipticus Illuminator	4
III	The Exponentially Tapered Transmission Line	6
	3.1 Input Impedance Derivation	6
	3.2 Transition Section Design	11
	3.3 NEC Modeling	14
	3.4 Ohmic Losses	18
	3.5 Characteristic Impedance Computation	23
	3.6 Design and Construction of the Exponentially Tapered Transmission Line	31
IV	Computations and Experimental Testing	34
	4.1 Incident Electric Field Computation	34
	4.2 Measured Antenna Power Patterns	49
	4.3 Input Impedance Calculation	64
	4.4 Input impedance Measurement	64
	4.5 Current Computation	65
V	Conclusion	71
	References	72

I Introduction

1.1 Background

The present EMP test facilities at the Weapons Laboratory do not provide the required high frequency illumination. It has been proposed that a low level CW facility, incorporating the Ellipticus antenna, be used to provide a horizontally polarized electric field to illuminate test objects [1,2]. The original design specifications for the Ellipticus provided for an operating frequency range of 10 KHz to 100 MHz. Upgrading the Ellipticus CW antenna design to cover higher frequencies may be accomplished by using a transition section from the driver to the antenna that radiates up to a few GHz. This design is based on an exponentially tapered transmission line design that has radiator characteristics at the high frequencies and serves as a matching section at low frequencies.

Due to the wide operating frequency range, a numerical rather than analytical analysis of the Ellipticus illuminator is required. A suitable procedure is developed that incorporates the NEC computer code [3]. Since the number of unknowns increases significantly with the frequency, a novel wire segmentation procedure is used [4]. This allows the analysis of very large wire configurations and provides sufficient accuracy with acceptable computer memory requirements and computational time.

1.2 Scope of the Investigations

In this report, efficient numerical solution techniques have been developed to examine the electromagnetic fields that can be developed in the working volume of the Ellipticus facility operated at frequencies from approximately 100 KHz to 1 GHz.

First, a detailed description of the Ellipticus CW antenna configuration design is given in order to perform a detailed analysis of the structure under study

[5].

Second, numerical models are developed to compute the fields in the working volume. The NEC code is used to analyze the Ellipticus configuration [3]. Features of the code include the treatment of a lossy ground plane, various impedance loading schemes, and several source models.

Third, the input transition section of the Ellipticus antenna for high frequency applications is designed. The basic design is accomplished by using exponentially tapered transmission line analysis. The NEC code is then used to evaluate the design in terms of the desired radiation pattern for the working volume. Also, a model of final design of the transition section is constructed and tested. The test, in general, includes radiation pattern testing and input impedance characterization.

Finally, a parametric study is performed to ascertain the performance of the Ellipticus illuminator for frequencies up to 1 GHz.

II Description of the Ellipticus Illuminator

Figures 2-1 and 2-2 [5] show the design structure of the CW Ellipticus antenna. The Ellipticus antenna configuration is a distributed impedance loaded wire structure where the wire forms one half of an ellipse, cut along the semi-major axis, over a lossy ground. The antenna is 100m across from the base and 20m at its highest point, a very large structure in terms of a wavelength at few Gigahertz.

The structure is driven from its highest point, at the center, by a differential mode CW driver thereby producing horizontal polarization of the electric field at the ground directly below the source. When a large object is illuminated, linear polarization is not expected over the entire surface. Typically, the test object is placed at the center of the Ellipticus antenna on the ground or raised off the ground on a rail car.

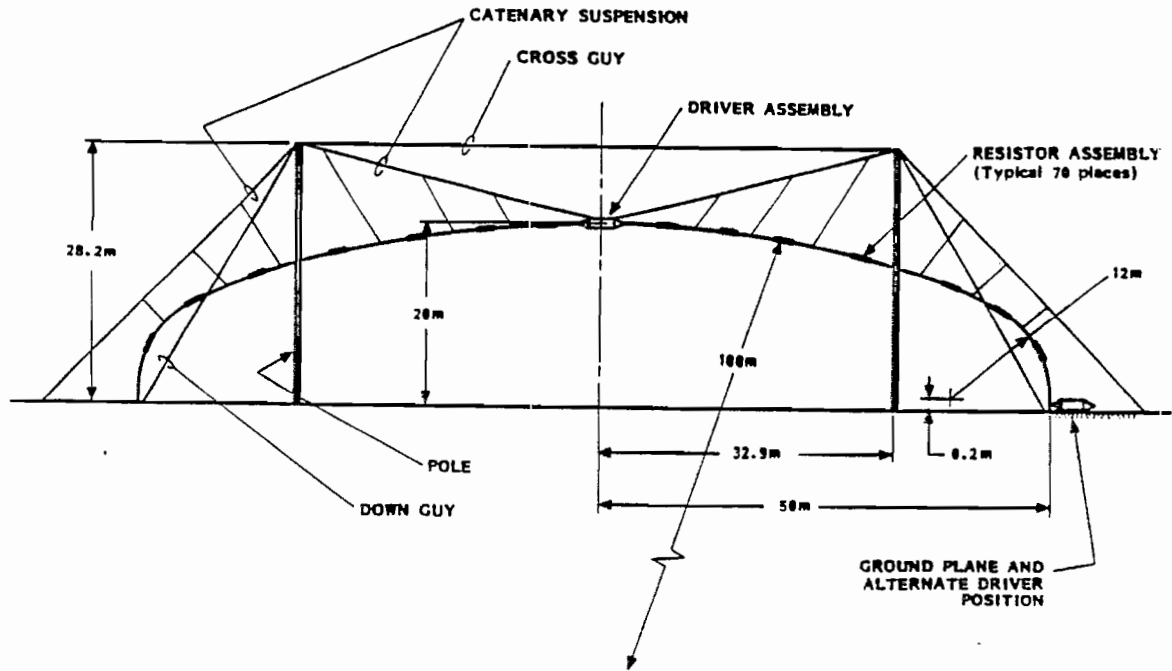


Figure 2-1: Ellipticus Elevation View

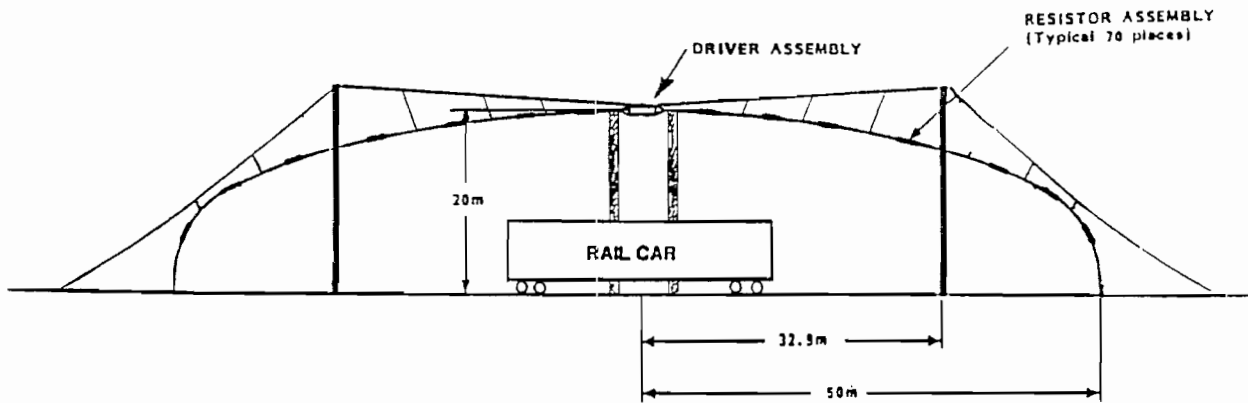


Figure 2-2: Ellipticus Configuration for Rail Cars

The antenna is constructed of 0.32 cm diameter, aircraft cable. The antenna is resistively loaded where the total antenna resistance is approximately 1750Ω , placed 0.1m apart along the length of the antenna.

III The Exponentially Tapered Transmission Line Design

3.1 Input Impedance Derivation

A transmission line whose impedance per unit length, Z , and admittance per unit length, Y , vary with distance down the line is known as a nonuniform transmission line. This transmission line is illustrated in Figure 3-1 below [6].

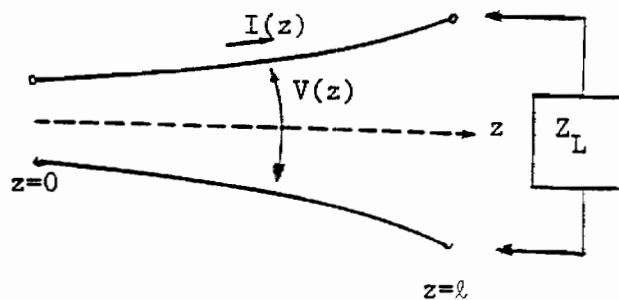


Figure 3-1: The Exponentially Tapered Transmission Line

One such nonuniform transmission line is the case in which Z and Y vary exponentially with distance down the line, z , as follows [6]:

$$Z(z) = j\omega L_0 e^{qz} \quad (3-1)$$

$$Y(z) = j\omega C_0 e^{-qz} \quad (3-2)$$

Note that L_0 and C_0 are the inductance and capacitance per unit length at the input, respectively. Also, q is the taper factor.

For an exponentially tapered transmission line (ETTL), the voltage and current vary with distance down the line, z , as follows:

$$V(z) = V_1 e^{-\gamma_1' z} + V_2 e^{-\gamma_1'' z} \quad (3-3)$$

$$I(z) = I_1 e^{-\gamma_2' z} + I_2 e^{-\gamma_2'' z} \quad (3-4)$$

where the subscripts 1 and 2 denote $+z$ and $-z$ traveling waves respectively and the exponent terms are defined as

$$\gamma'_{1,2} = \mp \frac{q}{2} + \sqrt{\left(\frac{q}{2}\right)^2 - \omega^2 L_0 C_0} \quad (3-5)$$

$$\gamma''_{1,2} = \mp \frac{q}{2} - \sqrt{\left(\frac{q}{2}\right)^2 - \omega^2 L_0 C_0} \quad (3-6)$$

Also, the differential equations for the variation of voltage and current along the transmission line are as follows:

$$\frac{dV(z)}{dz} = -Z(z)I(z) \quad (3-7a)$$

and

$$\frac{dI(z)}{dz} = -Y(z)V(z) \quad (3-7b)$$

From equation (3-4) and equation (3-7a), the $-z$ traveling current can be expressed as

$$I_2 e^{-\gamma_2'' z} = - \frac{1}{Z(z)} \frac{d}{dz} (V_2 e^{-\gamma_1'' z}) \quad (3-8)$$

By evaluating the derivative, the $-z$ traveling current can be solved for as

$$I_2 = \frac{V_2 \gamma_1''}{j\omega L_0} \quad (3-9)$$

Similarly, I_1 can be solved for as

$$I_1 = \frac{V_1 \gamma_1'}{j\omega L_0} \quad (3-10)$$

The input impedance to the transmission line can be expressed as

$$Z_{in} = \frac{V(0)}{I(0)} = \frac{V_1 + V_2}{I_1 + I_2} \quad (3-11)$$

Substituting I_1 and I_2 from equations (3-9) and (3-10) into equation (3-11) yields

$$Z_{in} = \frac{1 + \frac{V_1}{V_2}}{\frac{V_1}{V_2} + \frac{\gamma_1''}{\gamma_1'}} \left(\frac{j\omega L_0}{\gamma_1'} \right) \quad (3-12)$$

The characteristic impedance at any point z on the transmission line can be expressed as

$$Z_c(z) = \sqrt{\frac{Z(z)}{Y(z)}} = \sqrt{\frac{L_0}{C_0}} e^{\alpha z} \quad (3-13)$$

Note that $Z_c(z)$ does not represent the ratio of V/I for an infinite line.

The term under the radical in equations (3-5) and (3-6) can be designated as $j\beta$.
That is,

$$\beta = \sqrt{\omega^2 L_0 C_0 - \left(\frac{q}{2}\right)^2} \quad (3-14)$$

Letting $q=0$, which is true if the line has no tapering, equation (3-5) becomes

$$(for\ q=0) \quad \gamma'_{1,2} = j\omega\sqrt{L_0 C_0} = j\omega\sqrt{\mu_0 \epsilon_0} = j\beta_0 \quad (3-15)$$

Evaluating equation (3-13) at $z=0$, L_0 can then be solved as

$$L_0 = Z_c(0)\sqrt{\mu_0 \epsilon_0} \quad (3-16)$$

Finally, using equations (3-14), (3-16), and the term β_0 from equation (3-15), equation (3-12) for Z_{in} can be re-written as

$$Z_{in} = \frac{1 + \frac{V_1}{V_2}}{\frac{V_1}{V_2} + \frac{\gamma_1''}{\gamma_1'}} \left(\frac{j\beta_0}{-\frac{q}{2} + j\beta} \right) Z_c(0) \quad (3-17)$$

If an arbitrary load is placed on the transmission line at $z=\ell$ (as shown in Figure 3-1), the voltage and current on the line at this termination point will obey the following relationship

$$Z_L = \frac{V(\ell)}{I(\ell)} \quad (3-18)$$

where $V(\ell)$ and $I(\ell)$ are defined by equations (3-3) and (3-4) evaluated at $z=\ell$. Z_L can now be re-written as

$$Z_L = \frac{V(\ell)}{I(\ell)} = \frac{V_1 e^{-\gamma_1' \ell} + V_2 e^{-\gamma_1'' \ell}}{V_1 e^{-\gamma_1' \ell} + \frac{\gamma_1''}{\gamma_1'} V_2 e^{-\gamma_1'' \ell}} \left(\frac{j\omega L_0}{\gamma_1'} \right) \quad (3-19)$$

Solving for the ratio V_1/V_2 yields

$$\frac{V_1}{V_2} = \frac{e^{j2\beta l} \left[\left(\frac{j\beta_0}{-\frac{q}{2} + j\beta} \right) Z_c(0)e^{qt} - Z_L \frac{\gamma_1''}{\gamma_1'} \right]}{\left[Z_L - \left(\frac{j\beta_0}{-\frac{q}{2} + j\beta} \right) Z_c(0) e^{qt} \right]} \quad (3-20)$$

Thus, the input impedance to an exponentially tapered transmission line with input characteristic impedance $Z_c(0)$ and loaded with an arbitrary complex load Z_L can be calculated by solving for V_1/V_2 using equation (3-20) and then substituting this into equation (3-17).

The resulting equation (3-17) is a function of the complex load Z_L placed across the load terminals of the ETTL and of the design parameters of the ETTL itself, q and Z_{c0} . The NEC modeling of the results for the Elliptic Illuminator (EI) using the ETTL as a transition section give the impedance(s) seen by the voltage source(s) used in the numerical model. This data is to be used along with the Z_{in} equation derived above to compute the input impedance of the EI structure at several frequencies of interest.

In each case, Thevenin modeling of some or all of the ETTL transition section are used in the NEC model and the values of Z_L used in the Z_{in} equation are found as

$$Z_{SNEC} - Z_{th} = Z_L \quad (3-21)$$

where Z_{SNEC} is the NEC source impedance. When no symmetry is used in the model, the values of Z_{SNEC} can easily be seen from considering Figure 3-2. When symmetry is used, two Thevenin voltage sources and loads are used as shown in Figure 3-3. In this case, Z_L is found as

$$2Z_{SNEC} - Z_{th} = Z_L \quad (3-22)$$

Also, the value of ℓ in the Z_{in} equation will be the length of the ETTL that is modeled by its Thevenin equivalent circuit. For all cases, except the 200 MHz and higher frequency cases, the value of ℓ is 1.935m (indicating the entire ETTL transition section is being modeled with its Thevenin equivalent circuit). For the cases of 200 MHz and higher frequencies, the value for ℓ will be 1.935m less the length of the portion modeled by straight wire segments in the NEC model.

3.2 Transition Section Design

The governing equation for the characteristic impedance of the exponentially tapered transmission line is [6]

$$Z_c(z) = Z_{c0}e^{az} \quad (3-23)$$

where $Z_c(z)$ is the characteristic impedance at a point z on the line and Z_{c0} is the input characteristic impedance (i.e. at $z=0$). For this design $Z_{c0}=50$ ohms. Circular conductors of radius a will also be used for this design.

When the center-to-center wire spacing at a point z , $s(z)$, is at least several times the wire radius, the characteristic impedance for a two-wire transmission line can be approximated by [7]

$$\frac{\eta}{\pi} \ln \left[\frac{s(z)}{a} \right] = Z_c(z) \quad (3-24)$$

Equations (3-23) and (3-24) can be equated and their derivatives with respect to z can then be taken. Solving for $s'(z)$, that is the derivative with respect to z of $s(z)$, yields

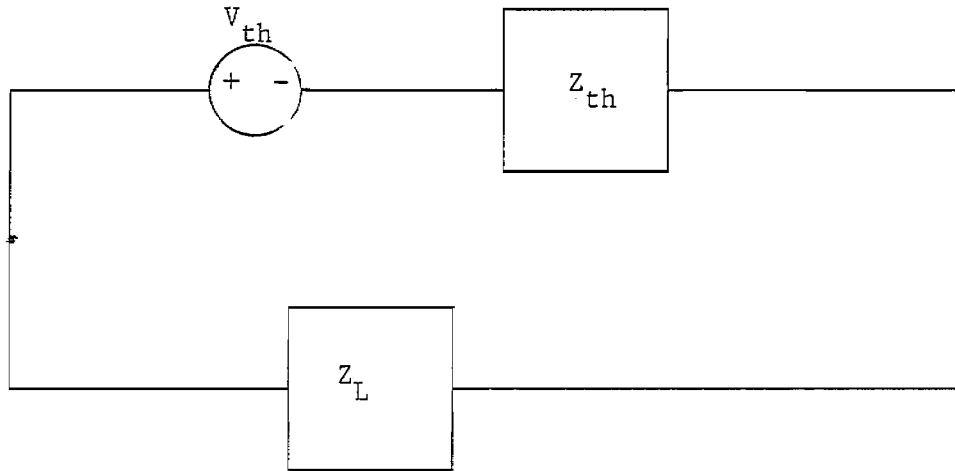


Figure 3-2: Basic Circuit Model of the EI When No Symmetry Is Used

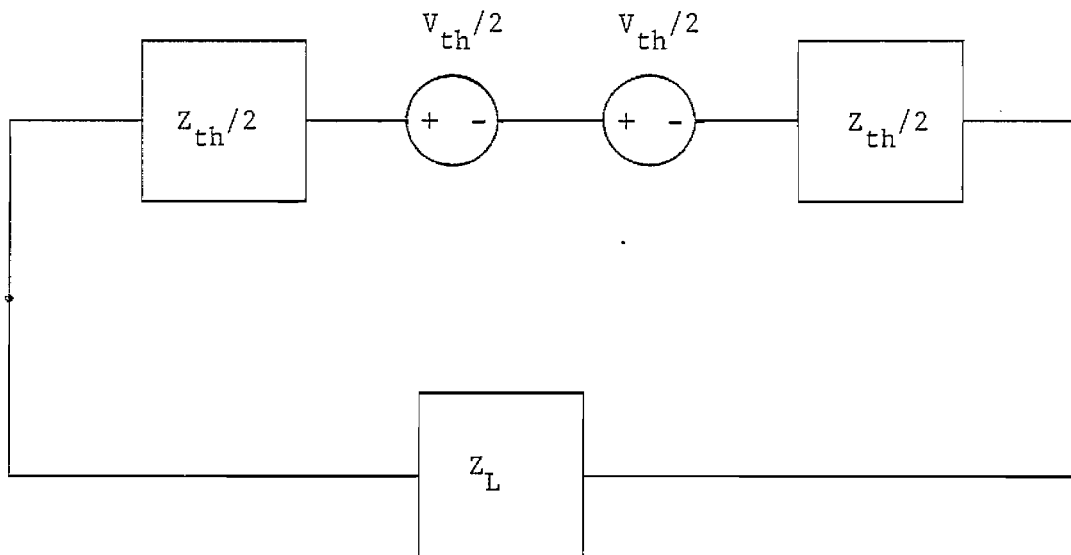


Figure 3-3: Basic Circuit Model of the EI when Symmetry Is Used

$$s'(z) = s(z) \frac{\pi Z_{c0}}{\eta} q e^{qz} = s(z) \frac{\pi Z_c}{\eta z} \ln \left(\frac{Z_c}{Z_{c0}} \right) \quad (3-25)$$

Solving for the position along the transmission line, z , yields

$$z = \frac{s(z)}{s'(z)} \frac{\pi Z_c}{\eta} \ln \left(\frac{Z_c}{Z_{c0}} \right) \quad (3-26)$$

In these expressions, the term $s'(z)$ is chosen as a constant value to begin the design. Figure 3-4 below illustrates the exponentially tapered transmission line used as a transition section.

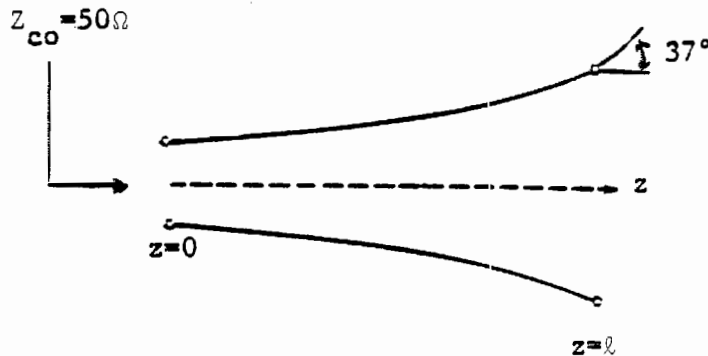


Figure 3-4: Transition Section

Choosing the 37 degree angle below yields $s'(l)=1.50711$.

Evaluating equation (3-24) at the end of the transition section, at $z=l$, and noting that $\eta=120\pi$ yields

$$Z_c(l) = 120 \ln \left[\frac{s(l)}{a} \right] \quad (3-27)$$

Evaluating equation (3-26) also at $z=\ell$ yields

$$\ell = \frac{s(\ell)Z_c(\ell)}{120 s'(\ell)} \ln \left[\frac{Z_c(\ell)}{Z_{co}} \right] \quad (3-28)$$

The design of the transition section can then be completed by choosing a value for $s(\ell)$ and computing the resulting $Z_c(\ell)$ and the length ℓ . Choosing $s(\ell)=0.4\text{m}$ yields $Z_c(\ell)=413.98$ ohms and $\ell=1.935\text{m}$. These were the values selected for the transition section design. These parameters for the transition section yield a 50Ω to 413.98Ω transition of characteristic impedance over its 1.935m length.

This transition section will also have a lower cutoff frequency that can be calculated as [6]

$$\omega_c = \frac{1}{\sqrt{L_0 C_0}} \left(\frac{q}{2} \right) \quad (3-29)$$

In equation (3-29) q can be solved for from equation (3-22). Using the design parameters mentioned above, this yields $q=1.0924$ and a cutoff frequency of $f_c=26.07$ MHz.

3.3 NEC Modeling

The exponentially tapered transmission line driven with a 1V source can be replaced by a Thevenin equivalent circuit for the portion from $z=0$ to $z=\ell'$, $\ell' \leq \ell$, as shown in Figure 3-5 below. This model will be accurate to use in the NEC model as long as the wire spacing of the transmission line at $z=\ell'$ is much less than one wavelength.

The Thevenin equivalent model will have $V_{th}=V_{oc}(\ell')$ and $Z_{th}=V_{oc}(\ell')/I_{sc}(\ell')$. Expressions for V_{th} and Z_{th} can be derived using the open circuit and short circuit conditions on the circuit of Figure 3-5 [8].

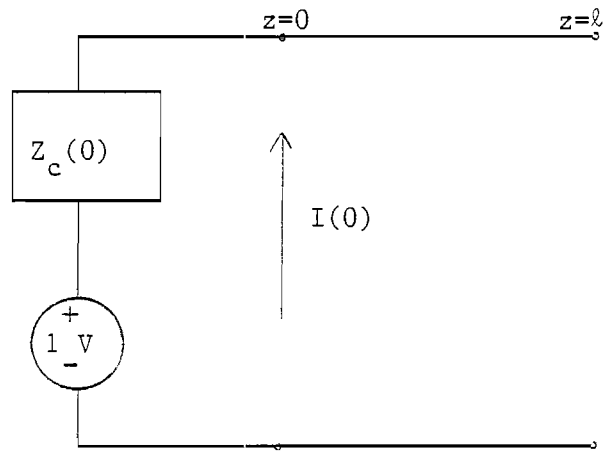


Figure 3-5: Thevenin Equivalent Circuit

The voltage and current on the exponentially tapered transmission line will obey the following relationships [6]

$$V(z) = V_1 e^{-\gamma_1' z} + V_2 e^{-\gamma_1'' z} \quad (3-30)$$

$$I(z) = \left(\frac{V_1 \gamma_1'}{j\omega L_0} \right) e^{-\gamma_1' z} + \left(\frac{V_2 \gamma_1''}{j\omega L_0} \right) e^{-\gamma_1'' z} \quad (3-31)$$

Under open circuit conditions, the voltage at $z=0$ and the current at $z=l'$ can be expressed as

$$V(0) = 1 - I(0)Z_c(0) \quad (3-32)$$

and

$$I(l) = 0 \quad (3-33)$$

Evaluating equation (3-31) at $z=l'$ and equating it with equation (3-33) yields

$$\left(\frac{V_1 \gamma_1'}{j\omega L_0} \right) e^{-\gamma_2' \ell'} = - \left(\frac{V_2 \gamma_1''}{j\omega L_0} \right) e^{-\gamma_2'' \ell'} \quad (3-34)$$

Evaluating equation (3-30) at $z=0$ and equating it with equation (3-32) yields

$$V_1 + V_2 = 1 - \frac{Z_c(0)}{j\omega L_0} (V_1 \gamma_1' + V_2 \gamma_1'') \quad (3-35)$$

Equations (3-34) and (3-35) can be used to generate expressions for V_1 and V_2 . These expressions will then be used in equation (3-30) with $z=\ell'$ to yield $V_{th}=V_{oc}(\ell')$.

From equation (3-35), V_1 can be found in terms of V_2 as

$$V_1 = \frac{1 - V_2 \left(1 + \frac{Z_c(0) \gamma_1''}{j\omega L_0} \right)}{\left(1 + \frac{Z_c(0) \gamma_1'}{j\omega L_0} \right)} \quad (3-36)$$

Substituting equation (3-36) for V_1 in equation (3-34) and solving for V_2 yields

$$V_2 = \left[\left(1 + \frac{Z_c(0) \gamma_1''}{j\omega L_0} \right) - \left(1 + \frac{Z_c(0) \gamma_1'}{j\omega L_0} \right) \left(\frac{\gamma_1''}{\gamma_1'} \right) e^{\ell' (\gamma_2' - \gamma_2'')} \right]^{-1} \quad (3-37)$$

To compute V_{th} for arbitrary values of $Z_c(0)$ and ℓ' , V_2 is first computed from equation (3-37), V_1 is then found from equation (3-36), and then V_{th} is found from equation (3-30) using $z=\ell'$.

Under short circuit conditions, equation (3-32) still holds and $V(\ell')=0$. Evaluating equation (3-30) at $z=\ell'$ and using the fact that $V(\ell')=0$ yields

$$V_1 e^{-\gamma_1' \ell'} = - V_2 e^{-\gamma_1'' \ell'} \quad (3-38)$$

Equation (3-38) above and equation (3-35), which is also valid for the short circuit

case, can be used to solve for V_1 and V_2 . These expressions will then be used in equation (3-31) at $z=\ell'$ to yield $I_{sc}(\ell')$. The relations for V_1 and V_2 are

$$V_1 = -V_2 e^{\ell'(\gamma_1' - \gamma_1'')} \quad (3-39)$$

and

$$V_2 = \left[\left(1 + \frac{Z_c(0)\gamma_1''}{j\omega L_0} \right) - \left(1 + \frac{Z_c(0)\gamma_1'}{j\omega L_0} \right) e^{\ell'(\gamma_1' - \gamma_1'')} \right]^{-1} \quad (3-40)$$

To compute $I_{sc}(\ell')$ for arbitrary values $Z_c(0)$ and ℓ' , V_2 is first computed from equation (3-40), V_1 is then computed from equation (3-39), and $I_{sc}(\ell')$ is computed from equation (3-31) at $z=\ell'$. Finally, Z_{th} is found as

$$Z_{th} = \frac{V_{oc}(\ell')}{I_{sc}(\ell')} \quad (3-41)$$

In the NEC modeling of the EI, the transition section is modeled by several straight wire sections that approximate the curvature of the ETTL. But due to limitations of the spacing of wires in the NEC program, the transition section is only modeled with straight wires up until the wire spacing approaches 4 or 5 wire radii in center-to-center separation. The remaining length of the transition section is denoted as ℓ' and is modeled with the Thevenin equivalent circuit previously discussed.

All of the EI except some or all of the transition section is modeled with straight wires. The coordinates for this wire model are taken from Figure 2-1 for the main EI's structure and from the tabulation of wire spacing, $s(z)$, as z varies for the transition section. These straight wire approximations to the lower portion of the transition section are used for the 200 MHz, 300 MHz, 500 MHz, 800 MHz, and 1 GHz cases. Figures 3-6 through 3-9 below are to-scale illustrations of these straight-wire approximations to the ETTL. Straight wires are used between the

is shown beside the wire. Symmetry about the x-z plane is used in these models, so only half of the ETTL is illustrated.

In addition to using Thevenin equivalent circuits to model portions of the transition section and using symmetry with the x-z plane, the EI is also modeled over a lossy ground plane. The Sommerfeld/Norton method for analyzing wire structures near a lossy ground plane is used in the NEC computations. For each frequency used, a program titled SOMNEC is run to generate a data file containing parameters of the lossy ground plane. This program is given the frequency of operation and the permittivity and conductivity of the ground plane in order to generate each output file. The data file is then used by the NEC program as it is running [5]. The permittivity and conductivity values used are for concrete. They are obtained from data in a publication by Castillo and Singaraju [9]. Their constitutive parameter data is given only up to a frequency of 100 MHz, so for higher frequencies the plots are extrapolated to obtain approximate values of the parameters up to a frequency of 1 GHz [10].

3.4 Ohmic Losses

The resistance per unit length of a transmission line increases significantly at high frequencies since the skin depth δ becomes small, i.e.,

$$\delta = \sqrt{\frac{2}{\omega\mu\sigma}} \quad (3-42)$$

where ω is the radian frequency, μ is the permeability, and σ is the conductivity. For most practical purposes, only that portion of a conductor that is within a skin depth of the surface carries significant current.

For a two-wire line with circular cross section conductors, the internal impedance per unit length is [11]

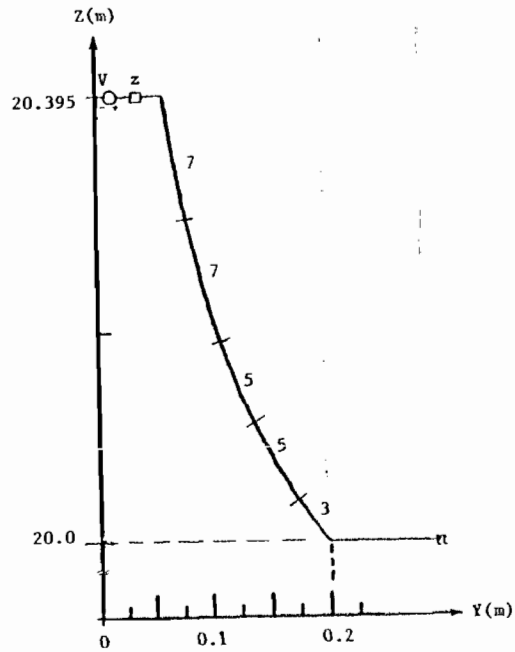


Figure 3-6: Straight-Wire Approximation to the Lower Portion of the Transition Section with Thevenin Equivalent Circuit Modeling of the Upper Portion at 200 MHz.
 $V = V_{ut}/2$ and $Z = Z_{ut}/2$

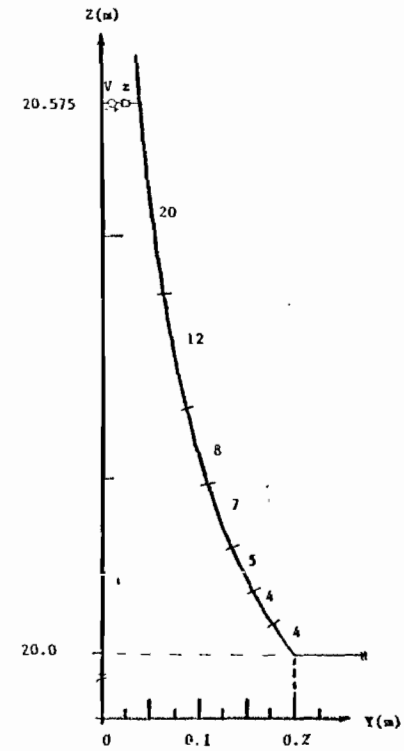


Figure 3-7: Straight-Wire Approximation to the Lower Portion of the Transition Section with Thevenin Equivalent Circuit Modeling of the Upper Portion at 300 MHz.
 $V = V_{ut}/2$ and $Z = Z_{ut}/2$

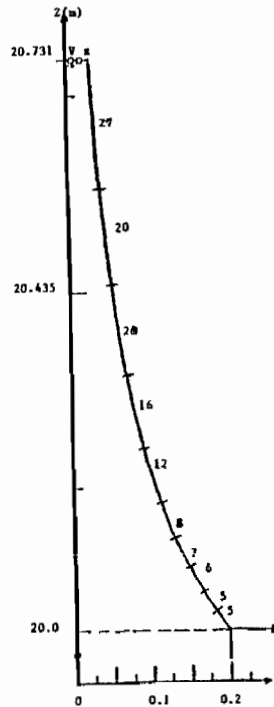


Figure 3-8: Straight-Wire Approximation to the Lower Portion of the Transition Section with Thevenin Equivalent Circuit Modeling of the Upper Portion at 500 MHz.
 $V = V_{th}/2$ and $Z = Z_{th}/2$

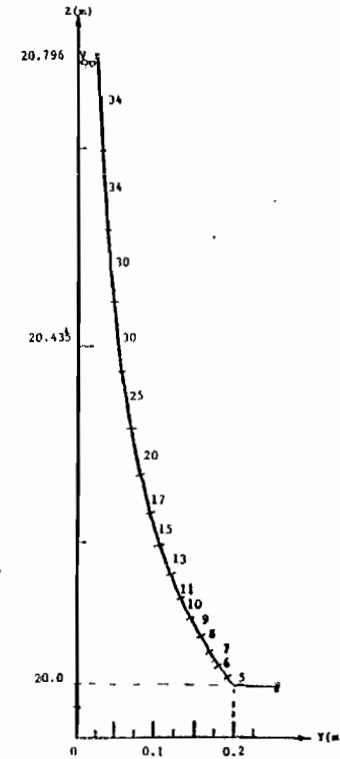


Figure 3-9: Straight-Wire Approximation to the Lower Portion of the Transition Section with Thevenin Equivalent Circuit Modeling of the Upper Portion at 1 GHz.
 $V = V_{th}/2$ and $Z = Z_{th}/2$

$$z^i|_{wires} = \frac{1+j}{\pi a} \sqrt{\frac{\omega \mu}{2\sigma[1 - (\frac{a}{h})^2]}} \quad (3-43)$$

where a is the wire radius and $2h$ is the center-to-center wire separation. Here, the real part of z^i is the wire resistance per unit length and the imaginary part is the inductance per unit length that arises from the magnetic flux inside the wire. Note that the internal impedance grows without bound as the wire separation approaches zero. This occurs because the line current tends to accumulate on the portion of the wire surface nearest the other conductor.

If the characteristic impedance of the transmission line must be as small as 50Ω , then for an air dielectric, the spacing should be

$$\frac{h}{a} = \cosh\left[\frac{\pi Z_c}{120\pi}\right] = 1.08807$$

And from equation (3-43), the internal impedance is increased by a factor of 2.33 over the internal impedance for a line spacing satisfying $h^2 \gg a^2$. Moreover, the close spacing of the conductors aggravates the breakdown problem and makes the fabrication more difficult because the reduced tolerance in separation distance variations.

For thin flat parallel conductors, generally called two-conductor strip line, the internal impedance is [12]

$$z^i|_{strips} = \frac{2(1+j)}{w} \sqrt{\frac{\omega \mu}{2\sigma}} \frac{x[1+x+\pi-2\ln(\frac{\alpha}{2})]}{1+x+\ln(1+x)} \quad (3-45)$$

where

$$x = \frac{\pi w}{2h} \quad (3-46)$$

and

$$\alpha = \left(1 + \frac{t}{h}\right)^2 - 1 + \left(1 + \frac{t}{h}\right) \sqrt{\left(1 + \frac{t}{h}\right)^2 - 1} \quad (3-47)$$

Here w is the plate width, $2h$ is the plate separation, and t is the plate thickness. The characteristic impedance of the strip line is [12]:

$$Z_c = \sqrt{\frac{\mu}{\epsilon}} \frac{\pi}{1 + x + \ln(1 + x)} \quad (3-48)$$

In order to compare the loss characteristics of strip conductors to circular conductors, the width of the plates is constrained to have the same circumference, i.e.,

$$2w = 2\pi a$$

and the characteristic line impedances are required to be equal. With these conditions, the ratio of the internal impedances is

$$\frac{z^i|_{strips}}{z^i|_{wires}} = \frac{2x[1 + x + \pi - 2 \ln(\frac{\alpha}{2})]}{1 + x + \ln(1 + x)} \sqrt{1 - \left(\frac{a}{h}\right)^2} \quad (3-49)$$

Considering a 50Ω characteristic impedance, then $h/a = 1.08807$ for circular conductors and $x = \pi w/2h = 19.66$ for flat strip conductors. In addition, for the comparison, let

$$\frac{t}{h} = 2 \frac{t}{w} \frac{w}{2h} = 2 \left(\frac{2}{32}\right)(6.26) = 0.78$$

Then $\alpha = 4.79$. Using the foregoing in (7) yields

$$\frac{z^i|_{strips}}{z^i|_{wires}} = 14$$

Clearly for the parameters selected, the ohmic losses of the strip line greatly exceed those of the circular conductor, two-wire transmission line. This is expected since the current distribution on thin strip conductors is highly nonuniform with most of the current in narrow sections at the edges [13]. Consequently, it is desirable to use circular conductors whenever possible.

In the construction of the exponentially tapered transmission line, the conductor cross section is continuously varied from flat strips to circular cross sections as the characteristic impedance increases exponentially. This was done to increase the power handling capability and provide low ohmic loss characteristics.

3.5 Characteristic Impedance Computation

The potential at points near an arbitrarily shaped conductor can be computed numerically by using a finite difference approximation to Laplace's equation [14]. In the discussion that follows, this method is applied to an elliptical conductor near a perfect ground plane in order to compute the two dimensional potential distribution about the conductor. From this, the charge on the ground plane (which is equivalent to that on the conductor) is found, and from that the characteristic impedance of the conductor will ultimately be computed (also see section 3-6).

Applying this process requires that the plane in which the potential values are to be found be overlaid by a grid. The potentials are computed only at the points where the grid lines cross. Known boundary conditions are applied to grid points that fall on a boundary whose potential is already known. Such points are initialized to their known value and are kept at these values throughout the iteration process that follows. Other boundary conditions may also be used in the iteration process.

The iteration process sweeps across the grid of points, adjusting the values of the potentials with each pass. The accuracy of this process is limited by how fine the grid is and by how many iteration passes are allowed to occur before the process is stopped.

Figure 3-10 below shows the boundary conditions and grid that is used to compute the potential at points in the region around an elliptical conductor. The symmetry about the y axis in this problem is also utilized to arrive at boundary conditions along the y axis.

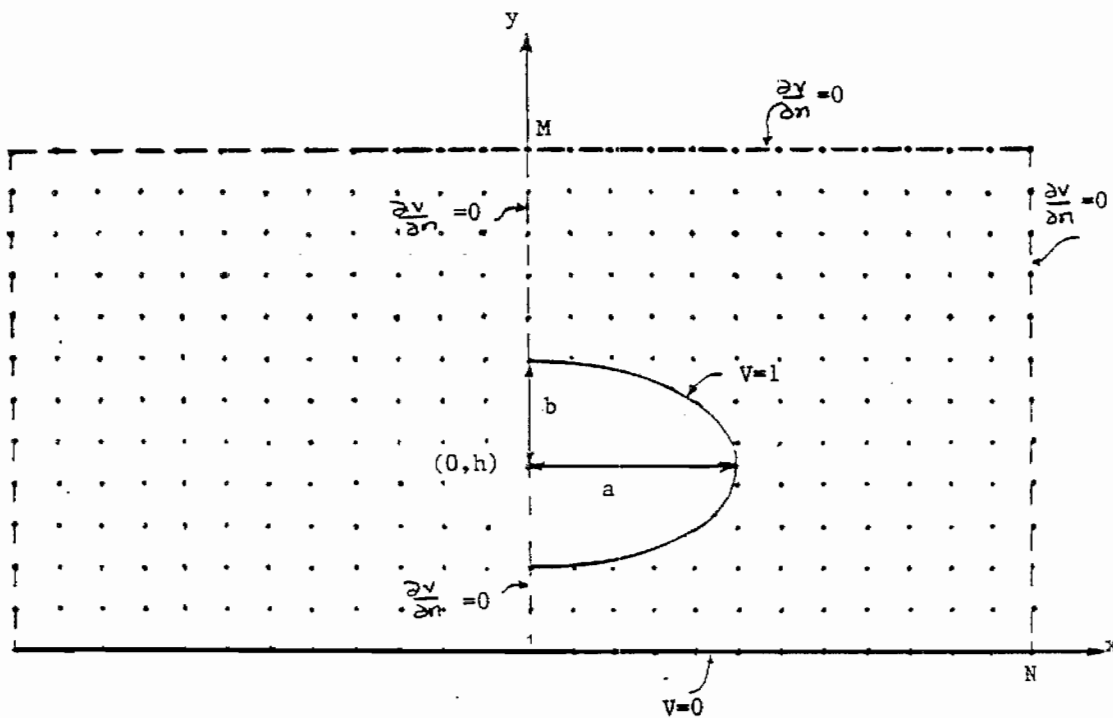


Figure 3-10: The Elliptical Conductor

The iterative process that is used in this problem is the successive overrelaxation (SOR) scheme. In this process, an arbitrary grid point (i,j) that does

not lie adjacent to a boundary is adjusted on the nth iterative pass to satisfy the following equation:

$$V_{ij}^{(n)} = (1-K)V_{ij}^{(n-1)} + \frac{K}{4} [V_{i+1j}^{(n-1)} + V_{i-1j}^{(n-1)} + V_{ij+1}^{(n-1)} + V_{ij-1}^{(n-1)}] \quad (3-50)$$

where $1 < K < 2$ and where V_{ij} is defined as

$$V_{ij} = V(x,y) \text{ where } x=i\Delta \text{ and } y=j\Delta \quad (3-51)$$

The values of K used most often are $1.1 < K < 1.3$ ($K=1.2$ is used in all of the production runs of this process in section 3-6).

In this case, a curved boundary is present. Many points that are adjacent to the curved boundary may have an adjacent point that falls on the other side of the curved boundary. Noting that the iterative equation (3-50) is a function of the potentials of the four adjacent points, equation (3-50) cannot be used in such cases. Instead, specialized iterative equations must be used when one or more of the four points adjacent to a grid point fall on or beyond a boundary.

For points that are close to the lower half of the curved boundary as shown in Figure 3-11, the iterative equation used is

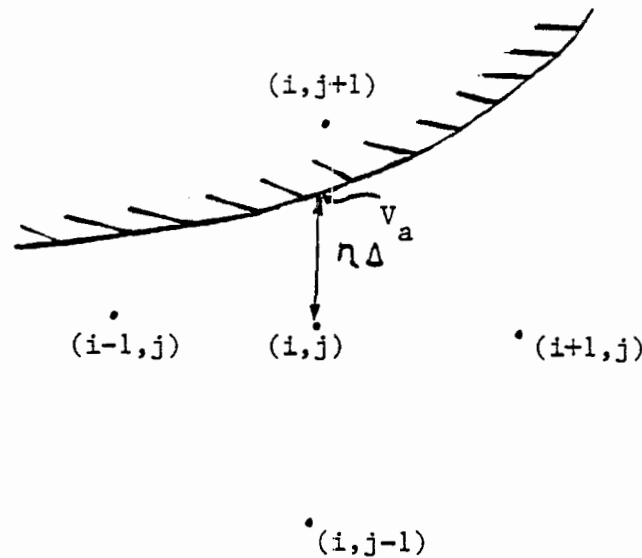


Figure 3-11: One Point Crossing the Boundary

$$V_{ij}^{(n)} = (1-K)V_{ij}^{(n-1)} + \frac{K}{1+\eta} \left\{ \frac{V_a}{1+\eta} + \frac{\eta}{1+\eta} V_{ij-1}^{(n)} + \frac{\eta}{2} [V_{i-1j}^{(n)} + V_{i+1j}^{(n-1)}] \right\} \quad (3-52)$$

where V_a is the value of the potential on the boundary as shown in Figure 3-11.

For points that are close enough to the boundary to have two adjacent points fall across the boundary, the iterative equation used is

$$V_{ij}^{(n)} = (1-K)V_{ij}^{(n-1)} + \frac{K}{\frac{1}{\xi} + \frac{1}{\eta}} \left\{ \frac{V_b}{\xi(1+\xi)} + \frac{V_a}{\eta(1+\eta)} + \frac{1}{1+\xi} V_{i+1j}^{(n-1)} + \frac{1}{1+\eta} V_{ij-1}^{(n)} \right\} \quad (3-53)$$

where V_a and V_b are the potentials on the boundary as shown in Figure 3-12.

Similar to the case of Figure 3-11 is that of Figure 3-13 below where one point crosses the boundary. In this case, the iterative equation used is

$$V_{ij}^{(n)} = (1-K)V_{ij}^{(n-1)} + \frac{K}{1+\xi} \left\{ \frac{V_b}{1+\xi} + \frac{\xi}{1+\xi} V_{i+1j}^{(n-1)} + \frac{\xi}{2} [V_{ij+1}^{(n-1)} + V_{ij-1}^{(n)}] \right\} \quad (3-54)$$

Here V_b is the potential on the boundary as shown in Figure 3-13.

Other possible configurations of points falling near the curved boundary are straight forward applications of the three cases already presented.

The other boundary conditions of Figure 3-10 involving the normal gradient of the potential being zero are easily implemented by setting the values of the potentials of the points that lie on these boundaries equal to that of the adjacent point that lies inside the grid. This is implemented by iterating points that lie near the boundary at $x=0$ as

$$V_{1j}^{(n)} = (1 - K) V_{1j}^{(n-1)} + \frac{K}{3} [V_{2j}^{(n-1)} + V_{1j+1}^{(n-1)} + V_{1j-1}^{(n)}] \quad (3-55)$$

Points that lie adjacent to the upper boundary are iterated as

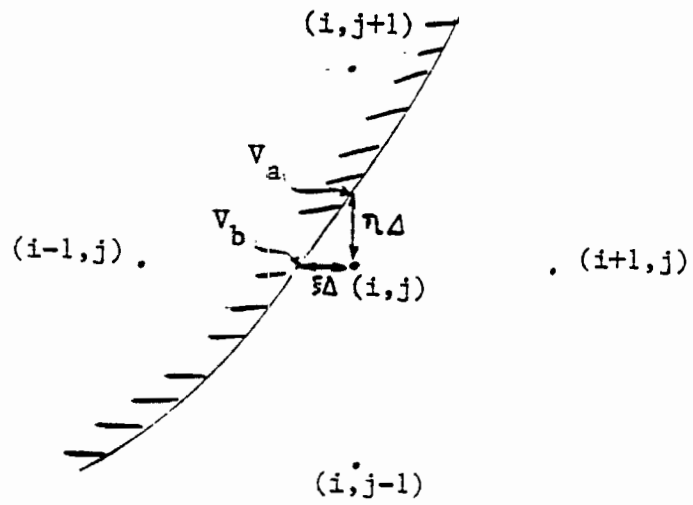


Figure 3-12: Two Points Crossing the Boundary

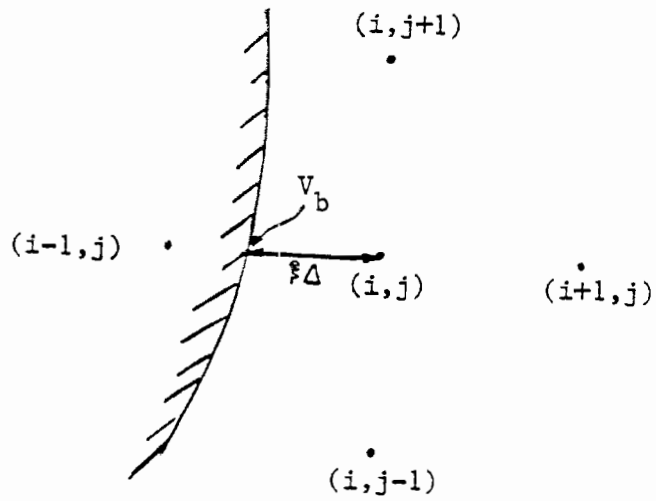


Figure 3-13: Second Case of One Point Crossing the Boundary

$$V_{i,M-1}^{(n)} = (1 - K) V_{i,M-1}^{(n-1)} + \frac{K}{3} [V_{i-1,M-1}^{(n)} + V_{i+1,M-1}^{(n-1)} + V_{i,M-2}^{(n)}] \quad (3-56)$$

Points that lie adjacent to the right boundary are iterated as

$$V_{N-1,j}^{(n)} = (1 - K) V_{N-1,j}^{(n-1)} + \frac{K}{3} [V_{N-2,j}^{(n)} + V_{N-1,j+1}^{(n-1)} + V_{N-1,j-1}^{(n)}] \quad (3-57)$$

The four corner points have unique iterative equations. These equations are

$$V_{1,1}^{(n)} = (1 - K) V_{1,1}^{(n-1)} + \frac{K}{3} [V_{2,1}^{(n-1)} + V_{1,2}^{(n-1)}] \quad (3-58)$$

$$V_{N-1,1}^{(n)} = (1 - K) V_{N-1,1}^{(n-1)} + \frac{K}{3} [V_{N-2,1}^{(n)} + V_{N-1,2}^{(n-1)}] \quad (3-59)$$

$$V_{1,M-1}^{(n)} = (1 - K) V_{1,M-1}^{(n-1)} + \frac{K}{2} [V_{1,M-2}^{(n)} + V_{2,M-1}^{(n-1)}] \quad (3-60)$$

$$V_{N-1,M-1}^{(n)} = (1 - K) V_{N-1,M-1}^{(n-1)} + \frac{K}{2} [V_{N-1,M-2}^{(n)} + V_{N-2,M-1}^{(n)}] \quad (3-61)$$

Two other unique points are those along the boundary at $x=0$ and adjacent to the curved boundary. Iterative equations for these are straight forward applications of the previously described cases.

The program implementing this procedure for the elliptical conductor of Figure 3-10 uses the finite difference technique. In this program, N and M are set equal to simplify the calculation of the charge on the ground plane. Also, the voltage on the elliptical boundary is set at a constant one volt to simplify the iterative equations. The results of the finite difference program have been verified using a circular conductor (with $a=b$). The exact solution for the potential at points near a circular conductor is known from basic field theory [15]. The potentials numerically arrived at by the finite difference program have been checked for

several points and have been found to be within a few percent of the exact values.

Caution must be used however to ensure that: (1) the upper and right boundaries are at least $3a$ to $4a$ away from the origin, (2) the height of the conductor, h , is small (such as 30% or less of the length of a side boundary), and (3) that the tolerance used for stopping the iteration, TOL, is small enough to require several iterations to occur before convergence to a solution. At least $6N$ or more iterations is a minimum number for an accurate solution for the potential distribution.

From basic field theory, the characteristic impedance of a lossless transmission line is

$$Z_c = \sqrt{\frac{L'}{C'}} \quad (3-62)$$

where L' and C' are the inductance and capacitance per unit length of the transmission line [16]. Also

$$L'C' = \mu\epsilon \quad (3-63)$$

Combining equations (3-62) and (3-63), Z_c can be expressed as

$$Z_c = \frac{\sqrt{\mu\epsilon}}{C'} \quad (3-64)$$

The charge per unit length on the transmission line can be expressed in terms of C' and the potential difference between the conductors, V_0 , as [16]

$$Q' = C'V_0 \quad (3-65)$$

In the case of Figure 3-10, V_0 is set at 1 volt. This yields $Q'=C'$, which then makes equation (3-64) become

$$Z_c = \frac{\sqrt{\mu\epsilon}}{Q'} \quad (3-66)$$

The charge per unit length on the elliptical conductor of Figure 3-10 can be found by integrating the normal derivative of the potential around the conductor to give

$$Q' = \oint \epsilon \frac{\partial V}{\partial n} dl \quad (3-67)$$

An easier approach, however, is to integrate the normal derivative of the potential across the ground plane below the conductor, since this charge is the same as that on the conductor. By choosing the values of M and N the same in the finite difference program, finding the charge can be done by simply summing the values of the potentials in the row just above the ground plane of Figure 3-10. Knowing the charge, the characteristic impedance of a two-wire transmission line composed of the elliptical conductors separated by the distance 2h is then computed. Image theory and the symmetry of Figure 3-10 are taken into account to yield the correct value for Z_c for the elliptical two-wire transmission line.

The results of the finite difference program have been confirmed by running the case of a circular conductor ($a=b$) close to a perfect ground plane, the characteristic impedance of which is known exactly. The resulting characteristic impedance was found to be within approximately 2% of the exact value. The programs have also been tested on an elliptical conductor with $b \ll a$, that is a nearly flat conductor. The resulting characteristic impedance was found again to be within a couple of percent of the theoretical value for an infinitely thin, flat conductor of the same dimensions.

3.6 Design and Construction Of The Exponentially Tapered Transmission Line

Equation (3-24) gives the characteristic impedance of a two-wire transmission line of circular conductors [7] and is repeated below.

$$Z_c(z) = \frac{\eta}{\pi} \ln \left[\frac{s(z)}{a} \right] \quad (3-68)$$

In this equation, $s(z)$ is the center-to-center wire spacing at a point z along the line and z is the wire radius. This expression is accurate only when $s(z) > 4a$. For the ETTL design arrived at in section 3-2, this 4 radii separation point yields a characteristic impedance approximately 157.9Ω and occurs at $z=1.0528\text{m}$ from the 50Ω drive point. Thus, elliptically-shaped conductors are used from the drive point out to $z=1.0528\text{m}$. From $z=1.0528\text{m}$ to $z=1.935\text{m}$, where the transition section ends, circular conductors are used.

To arrive at final design parameters for the ETTL, the problem is divided into three sections: (1) from $z=0\text{m}$ to $z=1.05\text{m}$ where elliptical conductors are used, (2) from $z=1.05\text{m}$ to $z=1.254\text{m}$ where the conductors are circular but where an equation for $Z_c(z)$ more accurate equation (1) is used, and (3) from $z=1.254\text{m}$ to $z=1.935\text{m}$ where the conductors are circular and where equation (1) is used to calculate $Z_c(z)$. For the section with elliptical conductors, the finite difference method is run numerous times varying the ration b/a and the conductor center-to-center spacing $2h$. For each run, b and h are chosen arbitrarily and the semi-major axis length a is given by

$$a = \sqrt{\frac{c^2}{2\pi^2} - b^2} \quad (3-69)$$

where $c=0.0798\text{m}$, the circumference of a 1 inch outer diameter conductor. The circumference must me kept constant in all of these design runs of the finite difference routine.

Each resulting characteristic impedance computed by the finite difference process is then plotted based on where it would occur on the ETTL from equation (3-23). Thirteen cases are then chosen to yield a smooth increase in the ratio of b/a and the conductor center-to-center spacing $2h$. These cases are the first thirteen cases listed in Table 3-1 below.

From $z=1.05\text{m}$ to $z=1.254\text{m}$, the conductors of the ETTL are circular and their characteristic impedance is [15]

$$Z_c = \frac{\sqrt{\mu_0 \epsilon_0}}{C'} \quad (3-70)$$

where C' is the capacitance per unit length of the conductor given by

$$C' = \frac{\pi \epsilon_0}{\ln \left[\frac{(h + \sqrt{h^2 - b^2})}{b} \right]} \quad (3-71)$$

This equation is more accurate than that of equation (3-68) for the close conductor spacing that is involved in this portion of the ETTL.

From $z=1.254\text{m}$ to $z=1.935\text{m}$, the conductors of the ETTL are still circular. The characteristic impedances in this last portion of the ETTL are calculated from equation (3-68). The final design parameters for constructing the ETTL with $Z_c(0)=50\Omega$, $Z_c(1)=413.98\Omega$, and $q=1.0924$ are tabulated in Table 3-1 above. In Table 3-1, z is the distance along the z axis from the drive point, b is the length of the semi-minor axis of the elliptical conductor, a is the length of the semi-major axis, and $2h$ is the center-to-center conductor spacing of the ETTL.

The prototype ETTL is constructed from the design specifications of Table 3-1 with one exception. One inch outer diameter copper tubing is not a standard size, so 7/8" outer diameter copper tubing is substituted. The effects of this substitution should be minimal. For example, $Z_c(1)$ would be 430Ω rather than

Table 3-1 Example Design Parameters of the ETTL

<u>Z(m)</u>	<u>h (m)</u>	<u>a (m)</u>	<u>b (m)</u>	<u>Z_c (Ω)</u>
0.00000	0.004600	0.01746	0.00159	50.000
0.13300	0.005000	0.01746	0.00159	61.700
0.20000	0.005500	0.01746	0.00159	64.800
0.32000	0.006500	0.01785	0.00200	71.000
0.42000	0.008000	0.01771	0.00300	79.000
0.50000	0.009500	0.01751	0.00400	86.400
0.60000	0.011300	0.01725	0.00500	96.000
0.68000	0.013000	0.01693	0.00600	105.000
0.76000	0.015000	0.01654	0.00700	115.000
0.85000	0.017000	0.01608	0.00800	126.000
0.93000	0.019400	0.01554	0.00900	138.500
0.98000	0.021000	0.01492	0.01000	146.000
1.03600	0.023000	0.01420	0.01100	155.000
1.09100	0.026000	0.01270	0.01270	164.000
1.12700	0.028000	0.01270	0.01270	171.200
1.19600	0.031000	0.01270	0.01270	184.800
1.25400	0.034000	0.01270	0.01270	196.800
1.27500	0.0339883	0.01270	0.01270	201.307
1.30000	0.0356041	0.01270	0.01270	206.881
1.32500	0.0373448	0.01270	0.01270	212.609
1.35000	0.0392223	0.01270	0.01270	218.495
1.37500	0.0412502	0.01270	0.01270	224.544
1.40000	0.0434436	0.01270	0.01270	230.761
1.42500	0.0458193	0.01270	0.01270	237.150
1.45000	0.0483961	0.01270	0.01270	243.716
1.47500	0.0511954	0.01270	0.01270	250.463
1.50000	0.0542410	0.01270	0.01270	257.398
1.52500	0.0575598	0.01270	0.01270	264.524
1.55000	0.0611821	0.01270	0.01270	271.848
1.57500	0.0651424	0.01270	0.01270	279.374
1.60000	0.0694795	0.01270	0.01270	287.109
1.62500	0.0723780	0.01270	0.01270	295.058
1.65000	0.0794676	0.01270	0.01270	303.227
1.67500	0.0852263	0.01270	0.01270	311.623
1.70000	0.0915795	0.01270	0.01270	320.250
1.72500	0.0986024	0.01270	0.01270	329.117
1.75000	0.106381	0.01270	0.01270	338.229
1.77500	0.115015	0.01270	0.01270	347.593
1.80000	0.124619	0.01270	0.01270	357.217
1.82500	0.135325	0.01270	0.01270	367.107
1.85000	0.147286	0.01270	0.01270	377.271
1.87500	0.160681	0.01270	0.01270	387.716
1.90000	0.175717	0.01270	0.01270	398.450
1.92500	0.192636	0.01270	0.01270	409.482
1.95000	0.211723	0.01270	0.01270	420.819

413.98Ω, the length l would be 2.046m rather than 1.935m, and the cutoff frequency would be 25.09 MHz rather than 26.07 MHz. Any stretching of the tubing as it is flattened into an elliptical shape will further reduce these discrepancies.

Type L, 3/4" inner diameter, flexible copper tubing is used for the conductors of the ETTL. The tubing is flattened to closely approximate the elliptical conductors according to Table 3-1 specifications. The conductors are then secured to the edges of two 1" by 8" boards cut to set the proper spacing of the conductors. Countersunk woodscrews hold the conductors to the boards. A simple framework of 2" by 2" boards forms the support of the ETTL. An N-type feed-through connector is finally used to drive the ETTL. The finished prototype of the ETTL is shown in Figures 3-14 and 3-15 below.

IV Computations and Experimental Testing

4.1 Incident Electric Field Computation

To obtain the incident electric field along the ground plane in the working volume, numerical modeling of the EI is done using the NEC program. The structure is modeled over a lossy ground plane using Thevenin equivalent circuit models for portions of the transition section, as discussed in section 3-3. The desired data obtained from these numerical modeling experiments consist of the total electric and magnetic fields along line a at $x=6m$, $y=-15m$ to $0m$, $z=0m$ and line b at $x=4.705m$ to $7.295m$, $y=z=0m$, and at the origin. This is illustrated in Figure 4-1 below.

Given the x, y, and z components of both the total electric and magnetic fields, the incident field can be computed (approximating normal incidence on the ground plane) as follows [17]:

$$E_x^{inc} = \frac{1}{2} [E_x^{tot} - (120\pi) H_y^{tot}] \quad (4-1)$$

$$E_y^{inc} = \frac{1}{2} [E_y^{tot} + (120\pi) H_x^{tot}] \quad (4-2)$$

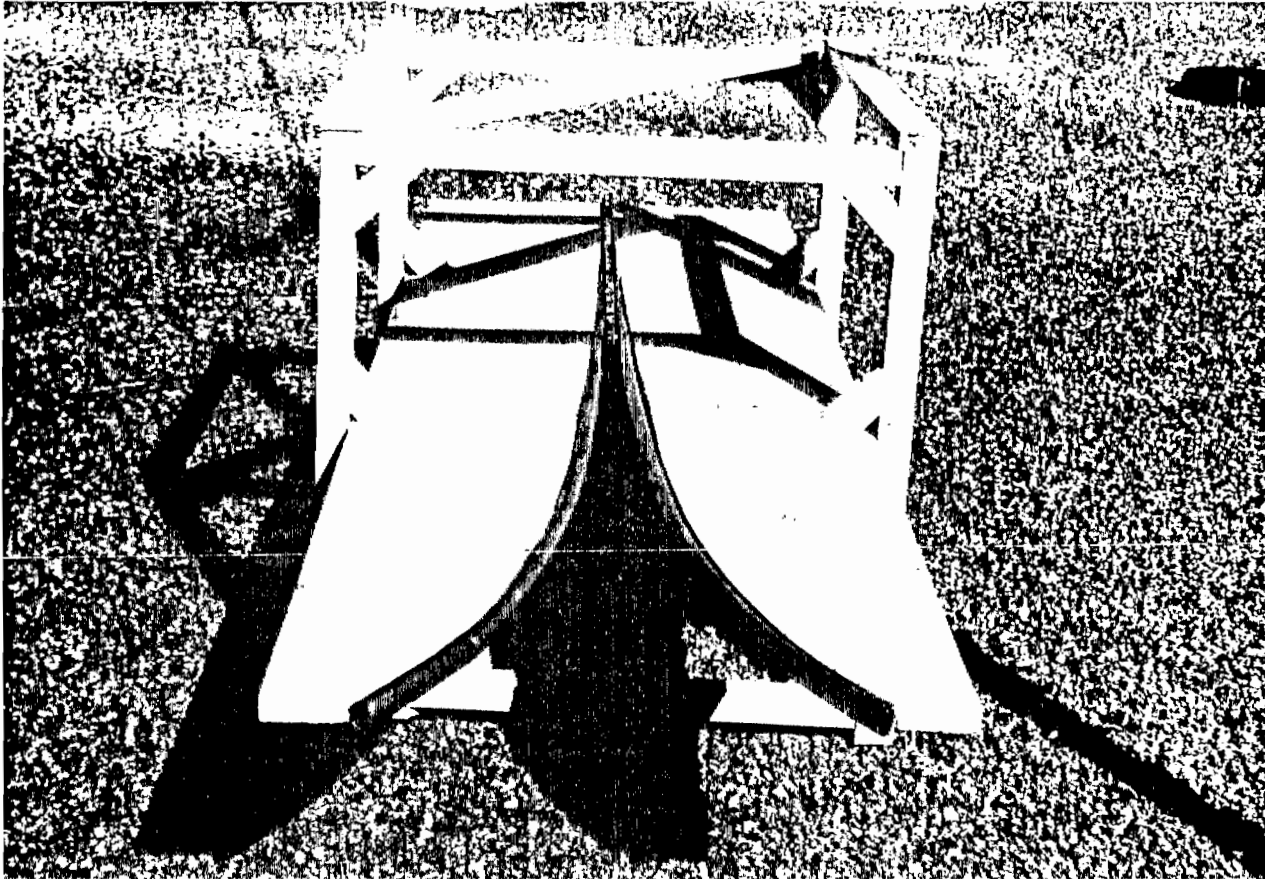


Figure 3-14: Prototype of the Exponentially Tapered Transmission Line (ETTL).

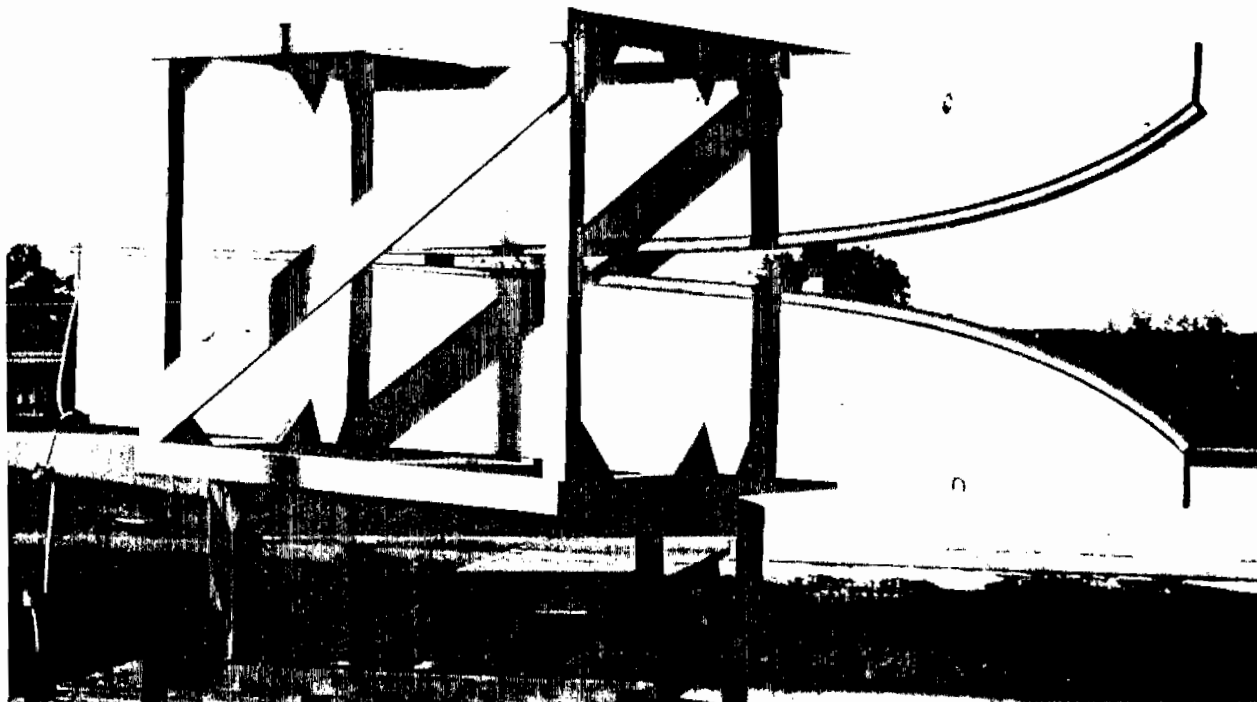


Figure 3-15: Prototype of the ETTL Undergoing Antenna Power Pattern Measurement.

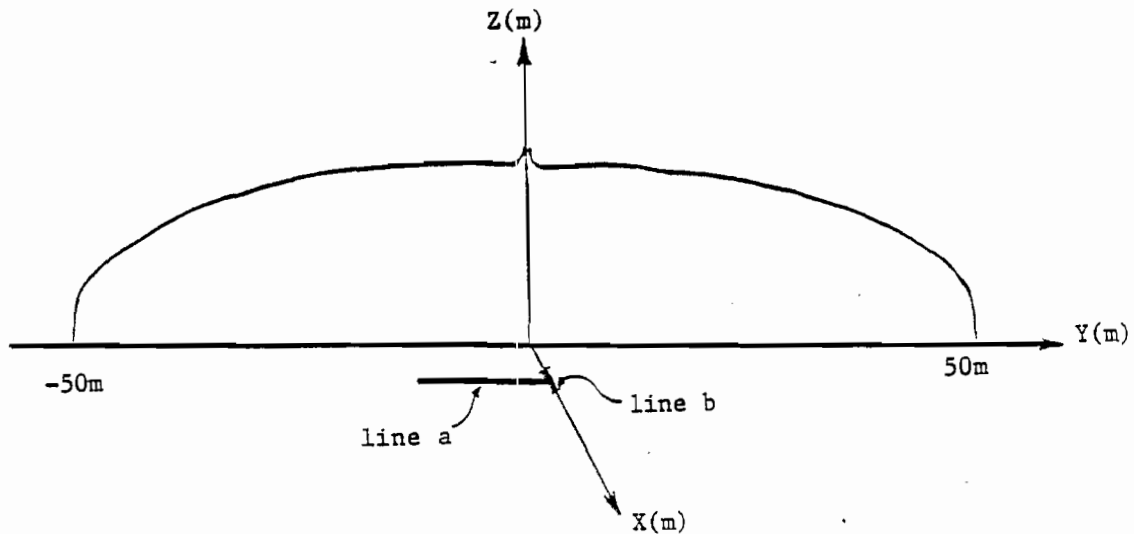


Figure 4-1: Lines Along which $|E_{inc}|$ Is Computed

These computations are performed for points 0.0625m apart along the line $x=6m$, $y=-15m$ to $0m$, $z=0m$ and for points 0.01047m apart along the line $x=4.705m$ to $7.295m$, $y=z=0m$. The magnitudes of the resulting incident electric field values are plotted to reveal the behavior of the incident field in this portion of the working volume. Ideally these plots should resemble the antenna pattern plots that are performed on the transition section alone for high frequencies.

Figures 4-2 through 4-21 illustrate the dominant y component of the incident electric field at 100 KHz, 500 KHz, 1 MHz, 5 MHz, 10 MHz, 100 MHz, 200 MHz, 300 MHz, 500 MHz, and 1 GHz along lines a and b of Figure 4-1.

Brief observations of these plots are summarized in Tables 4-1 and 4-2 below.

Table 4-1 Observations of the $|E_{inc}|$ plots
for the line a of Figure 4-1

<u>Frequency (MHz)</u>	<u>Approx. Range in Values of E_{inc}</u>	<u>Basic Description of the Curve</u>
0.1	1.05 to 1	smooth, constant slope
0.5	1.05 to 1	smooth, constant slope
1.0	1.09 to 1	smooth, constant slope
5.0	1.2 to 1	smooth, constant slope
10.0	1.24 to 1	smooth, constant slope
100.0	5.2 to 1	slow, smooth variations with sidelobes present
200.0	3.5 to 1	(same as for 100 MHz)
300.0	(large to a null)	slow, smooth variations with a deep null at $x \approx 10m$
500.0	1.2 to 1	slow, smooth variations
1000.0	2.5 to 1	rapid, small variations with a smooth envelope

Table 4-2 Observations of the $|E_{inc}|$ plots
for line b of Figure 4-2

<u>Frequency (MHz)</u>	<u>Approx. Range in Values of E_{inc}</u>	<u>Basic Description of the Curve</u>
0.1	1.07 to 1	essentially flat
0.5	1.07 to 1	essentially flat
1.0	1.07 to 1	essentially flat
5.0	1.08 to 1	essentially flat
10.0	1.06 to 1	essentially flat
100.0	1.06 to 1	essentially flat
200.0	1.07 to 1	essentially flat
300.0	1.11 to 1	essentially flat
500.0	1.21 to 1	essentially flat
1000.0	1.35 to 1	mostly flat but with slow, smooth variation

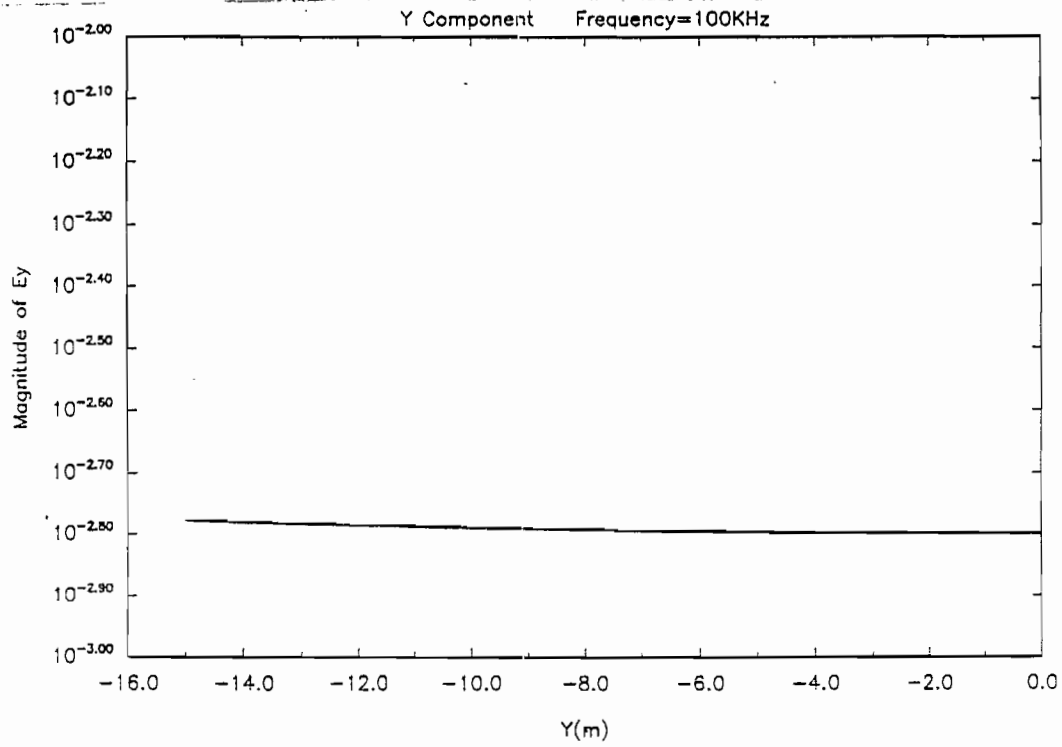


Figure 4-2: Incident E Field along Line x=6m and z=0m

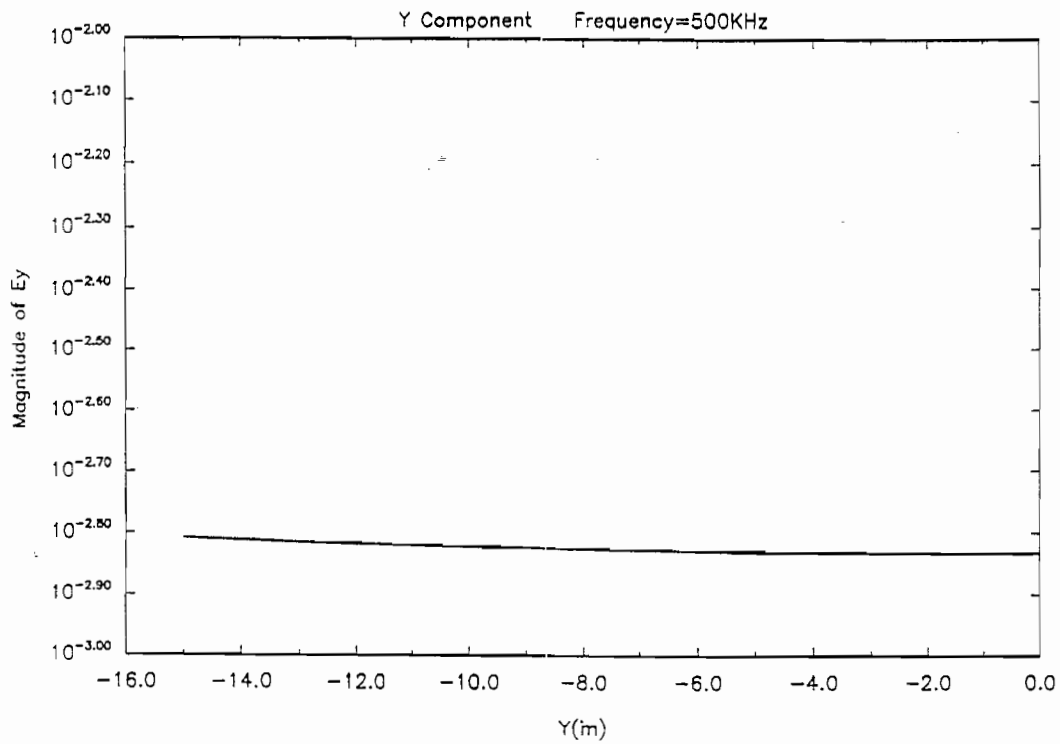


Figure 4-3: Incident E Field along Line x=6m and z=0m

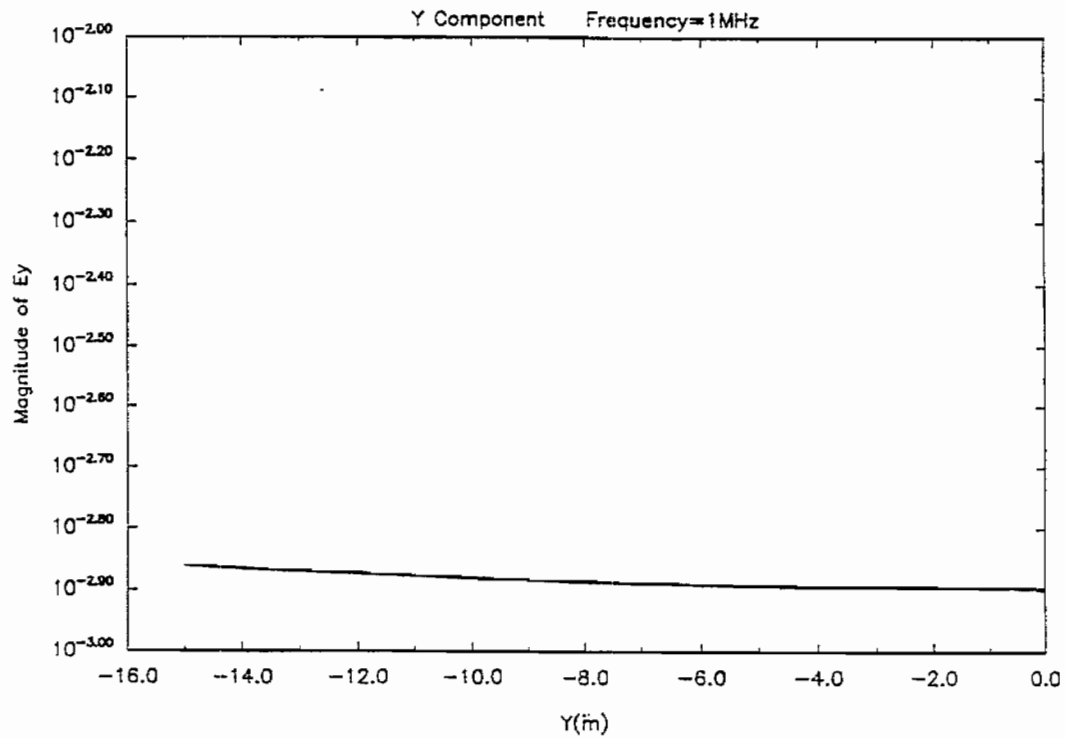


Figure 4-4: Incident E Field along Line x=6m and z=0m

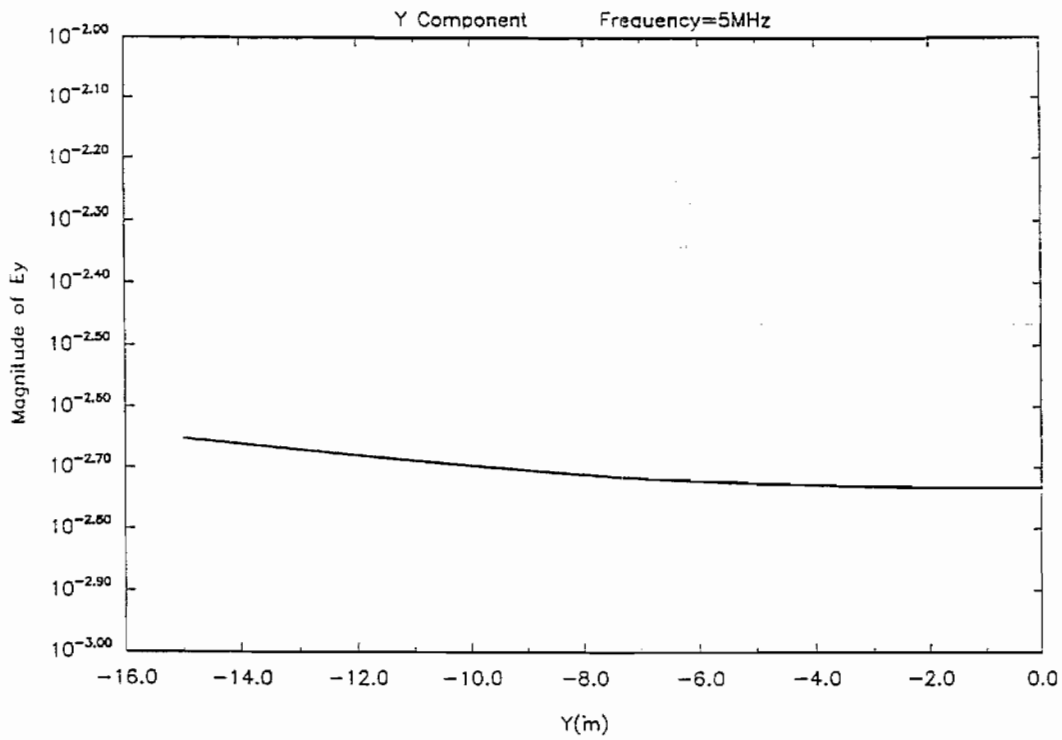


Figure 4-5: Incident E Field along Line x=6m and z=0m

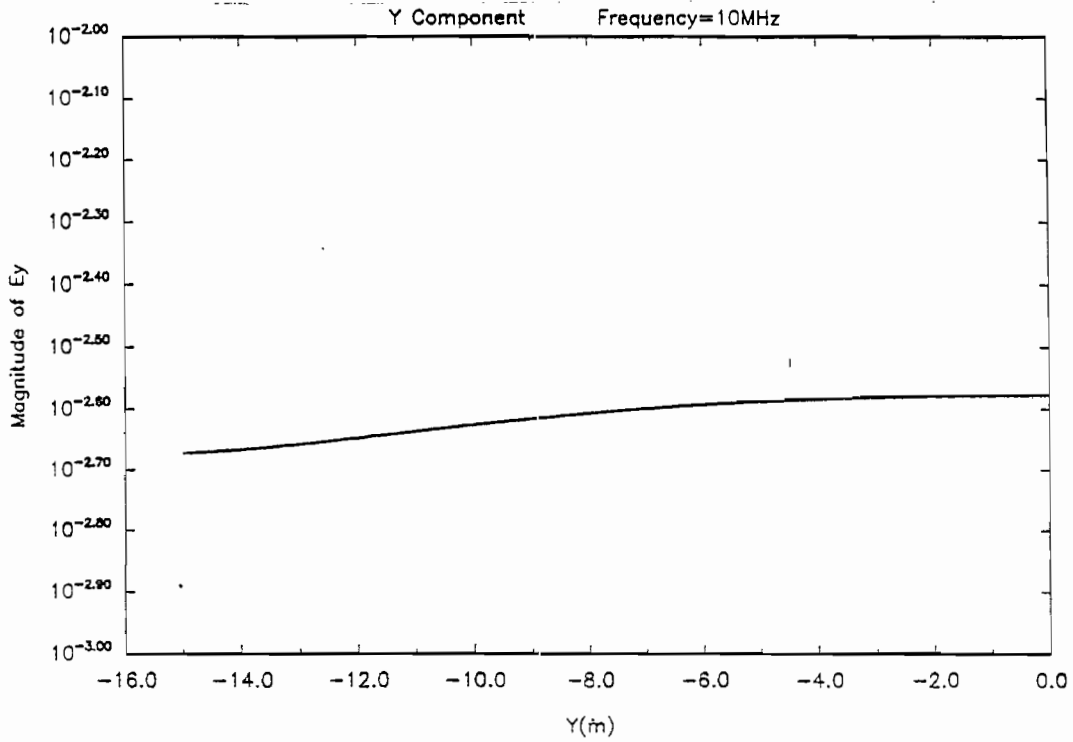


Figure 4-6: Incident E Field along Line x=6m and z=0m

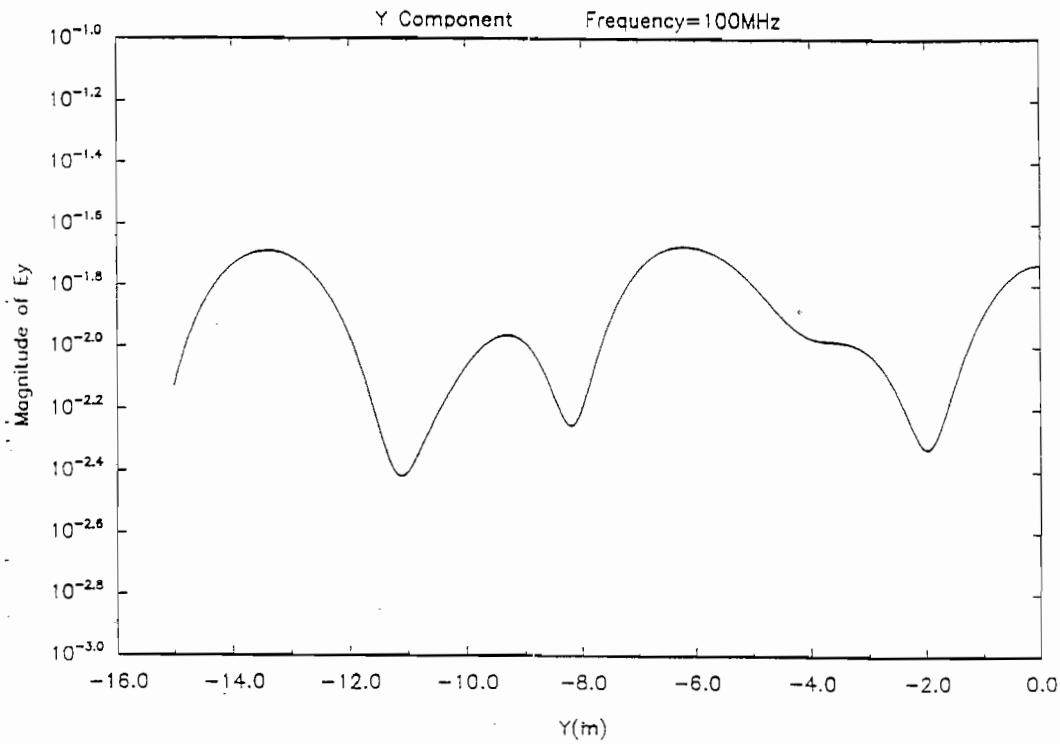


Figure 4-7: Incident E Field along Line x=6m and z=0m

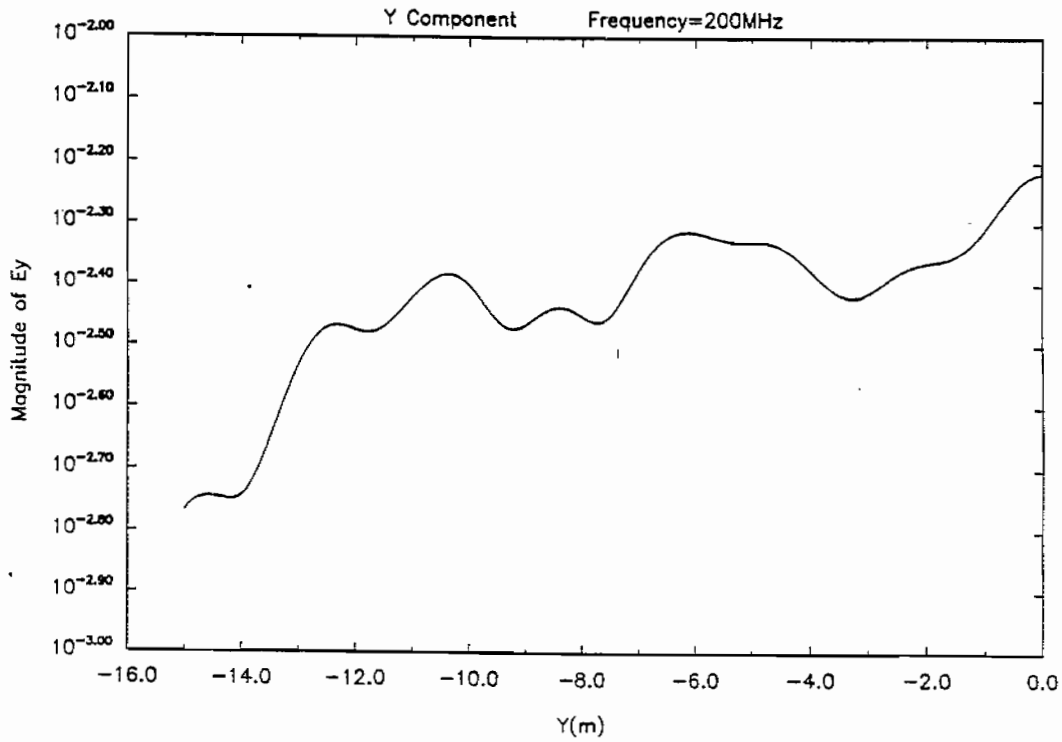


Figure 4-8: Incident E Field along Line $x=6m$ and $z=0m$

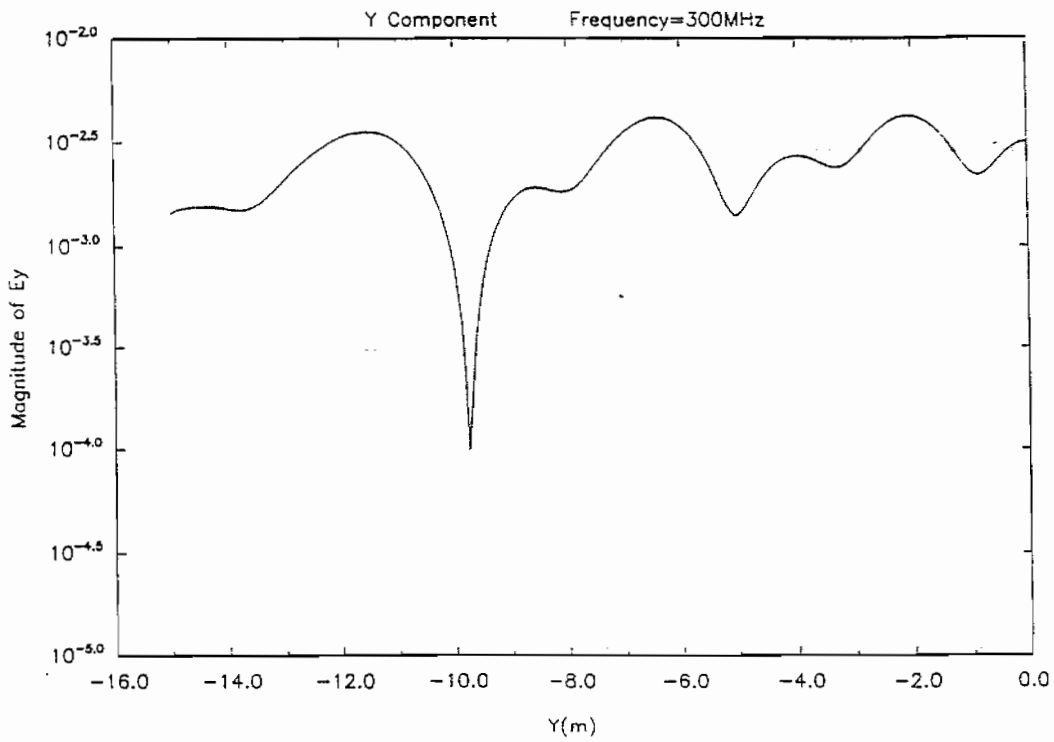


Figure 4-9: Incident E Field along Line $x=6m$ and $z=0m$

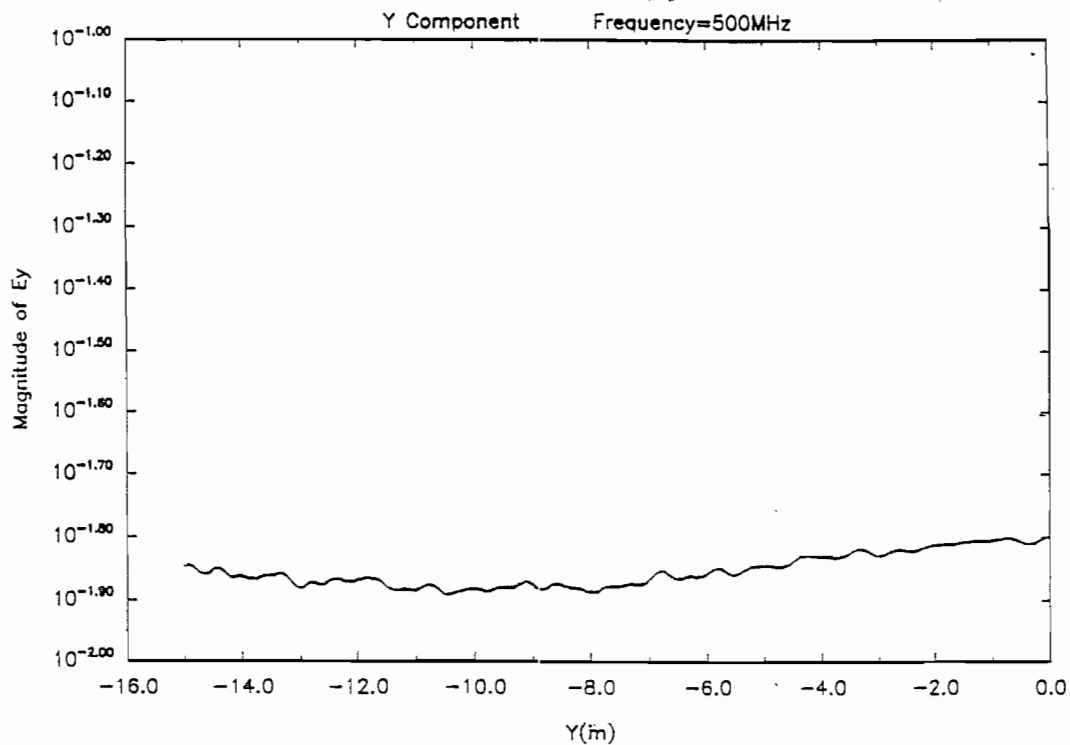


Figure 4-10: Incident E Field along Line $x=6m$ and $z=0m$

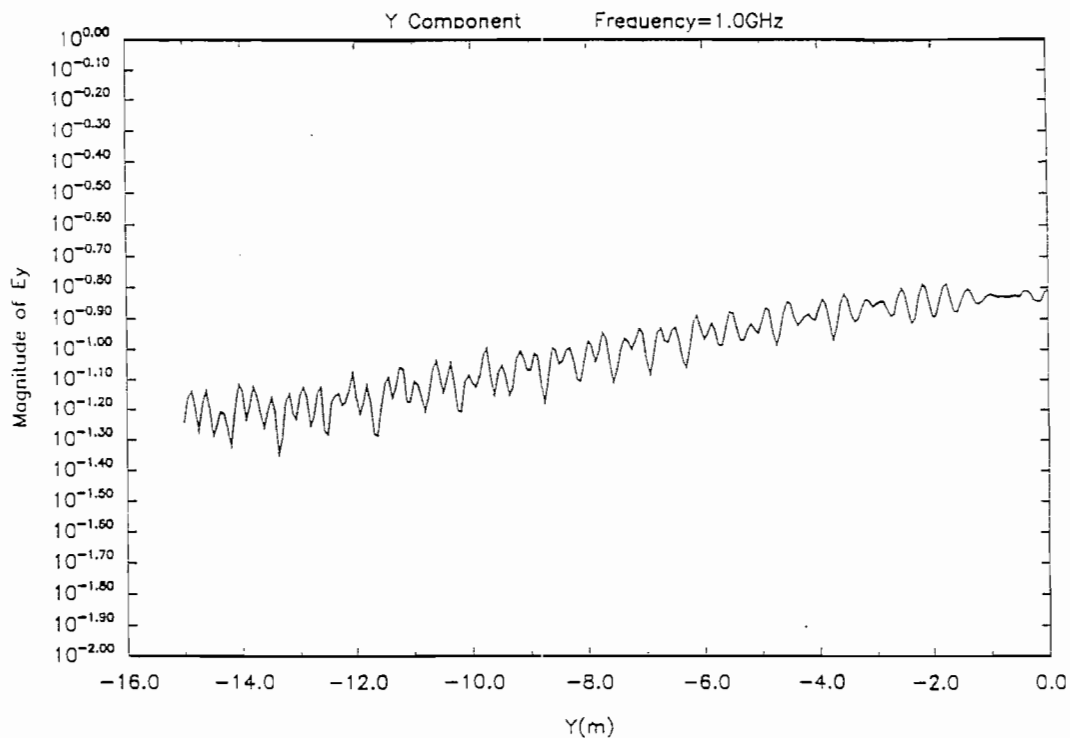


Figure 4-11: Incident E Field along Line $x=6m$ and $z=0m$

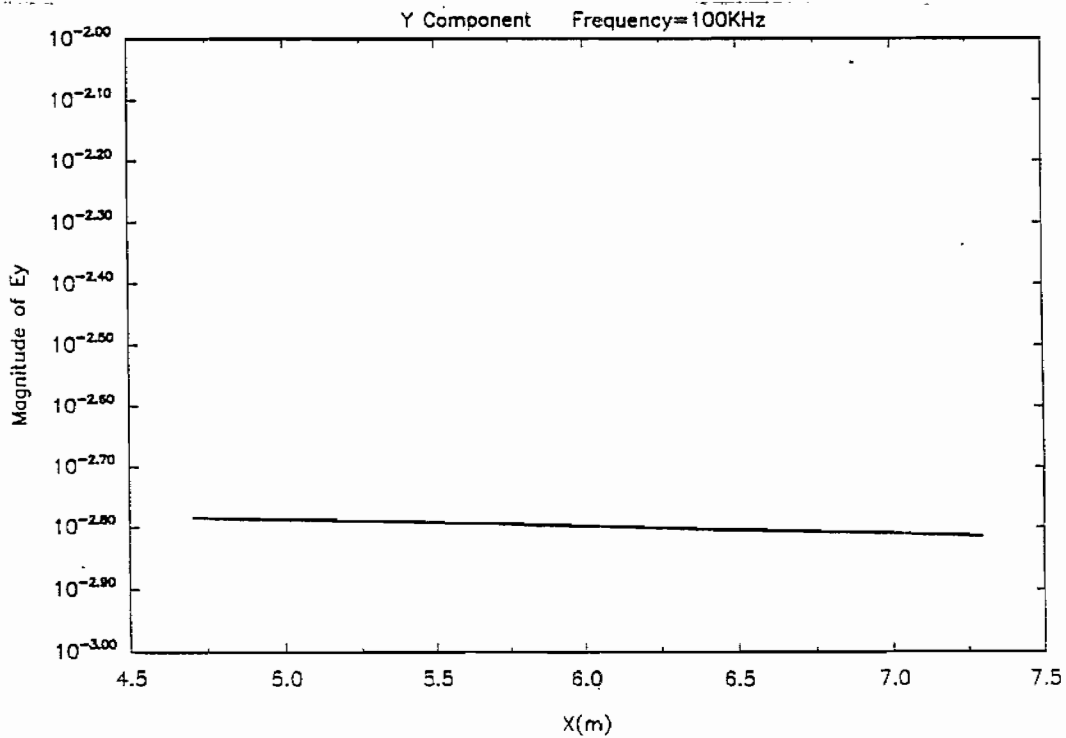


Figure 4-12: Incident E Field along Line y=0m and z=0m

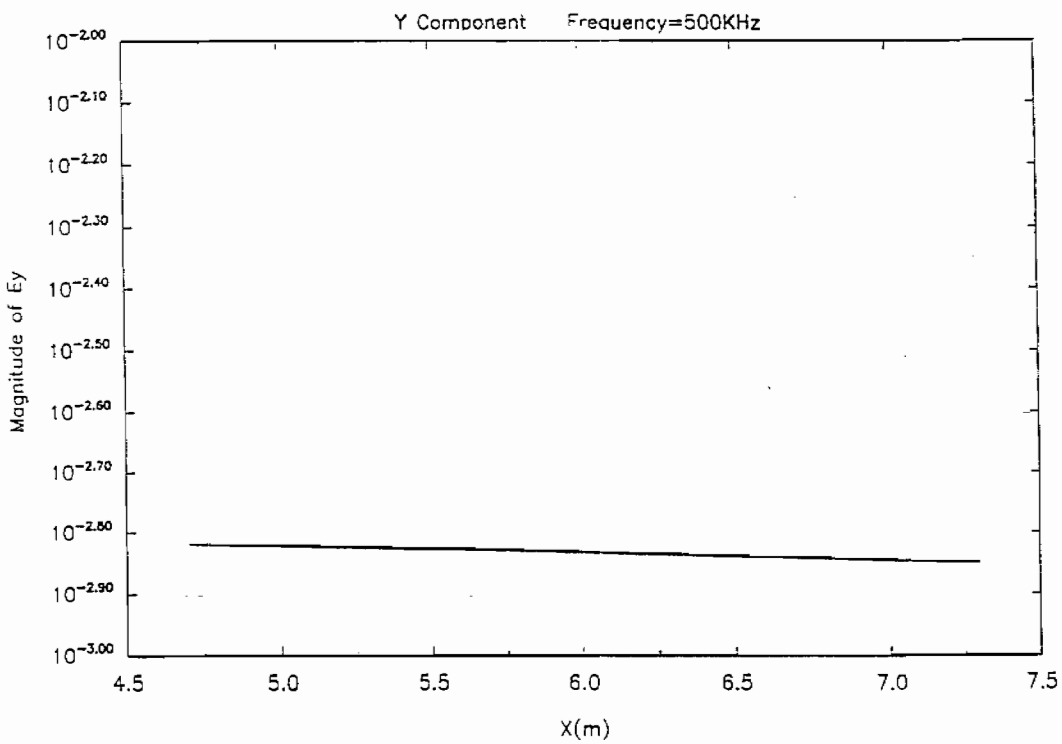


Figure 4-13: Incident E Field along Line y=0m and z=0m

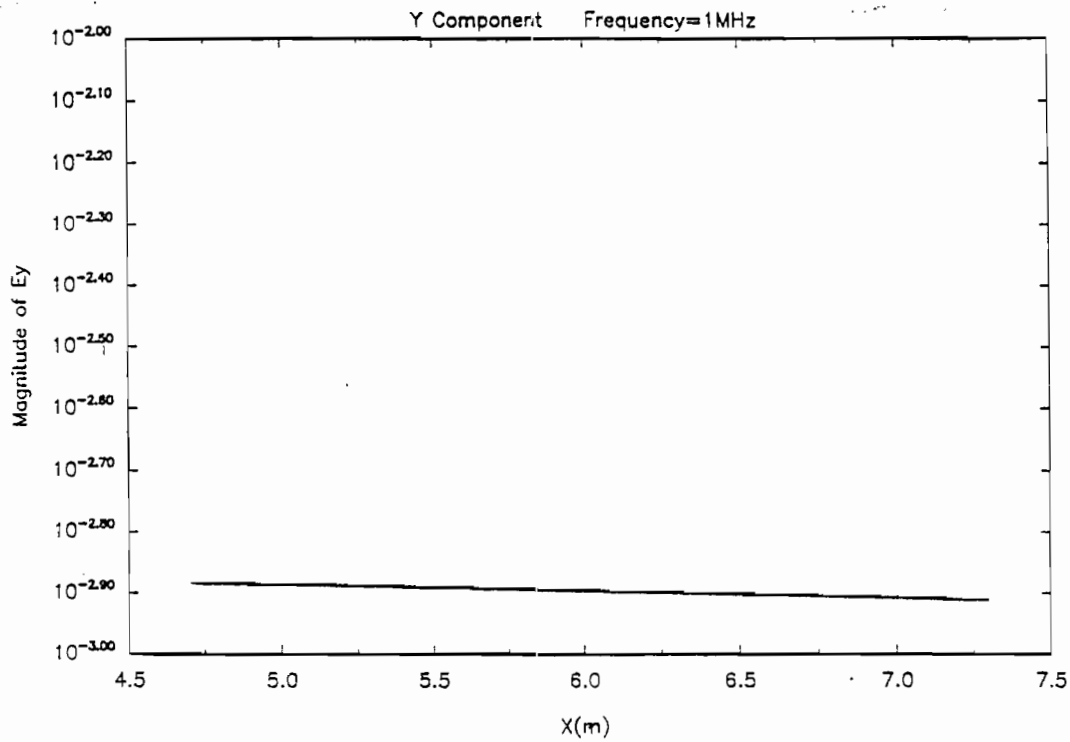


Figure 4-14: Incident E Field along Line $y=0m$ and $z=0m$

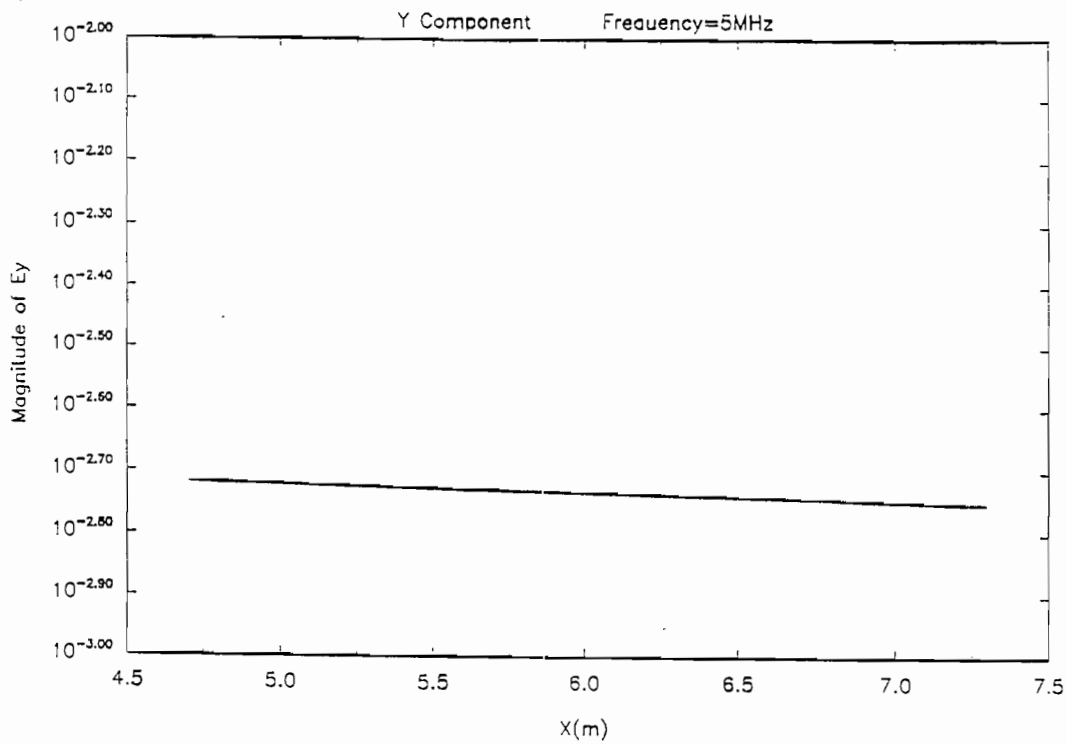


Figure 4-15: Incident E Field along Line $y=0m$ and $z=0m$

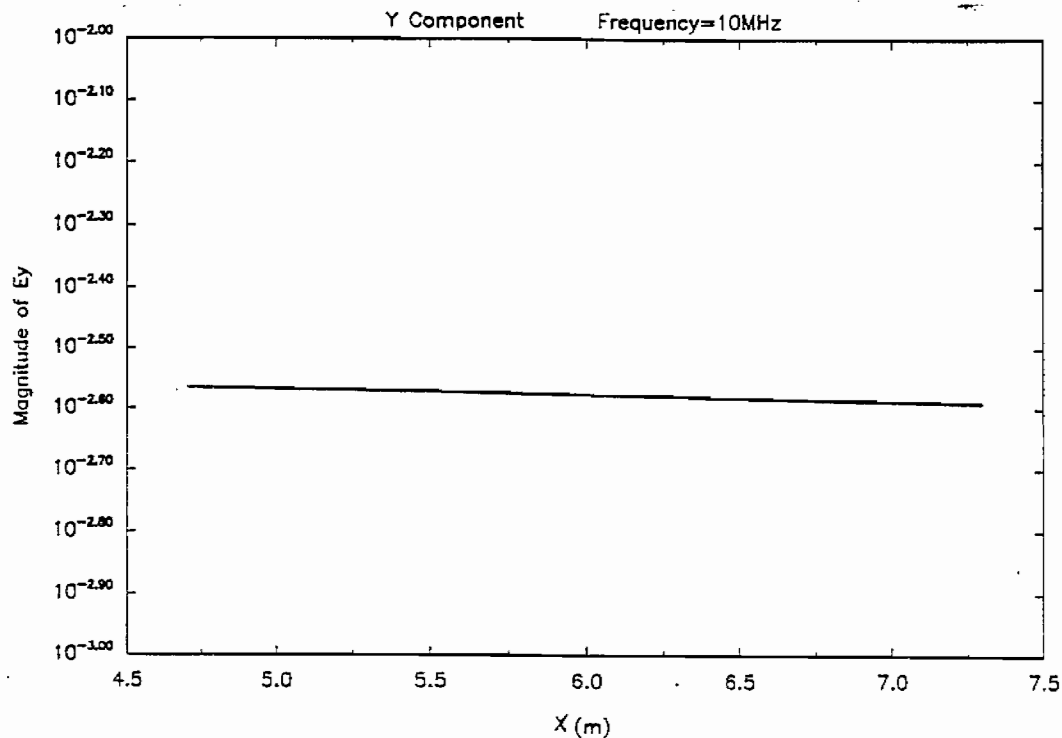


Figure 4-16: Incident E Field along Line $y=0m$ and $z=0m$

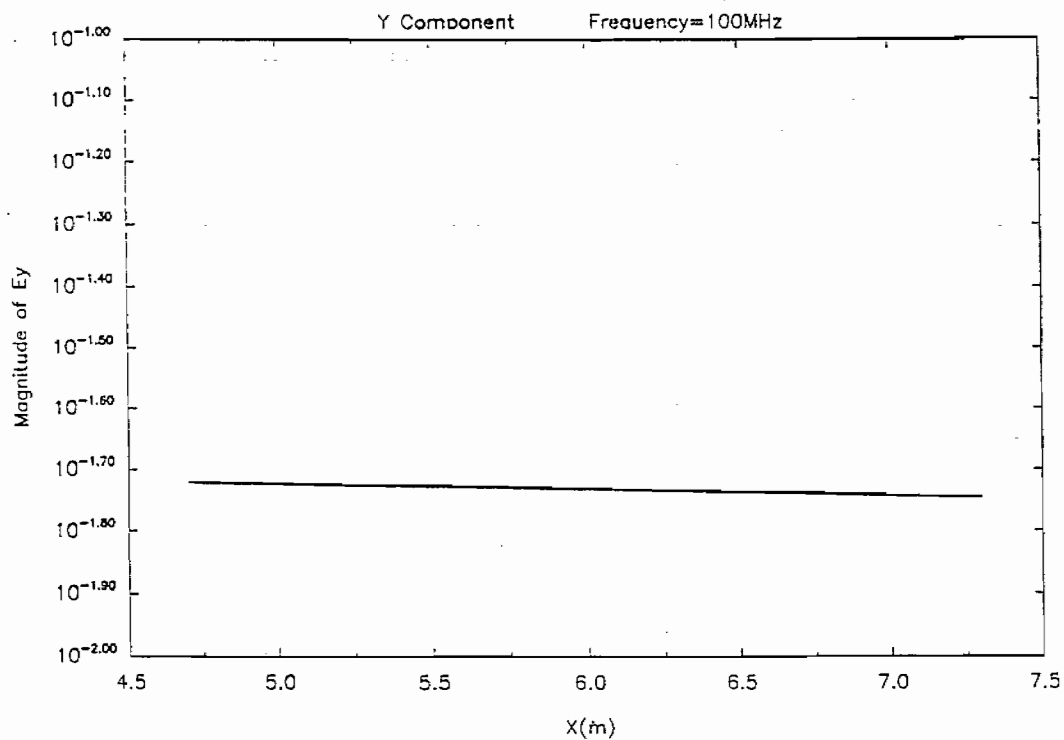


Figure 4-17: Incident E Field along Line $y=0m$ and $z=0m$

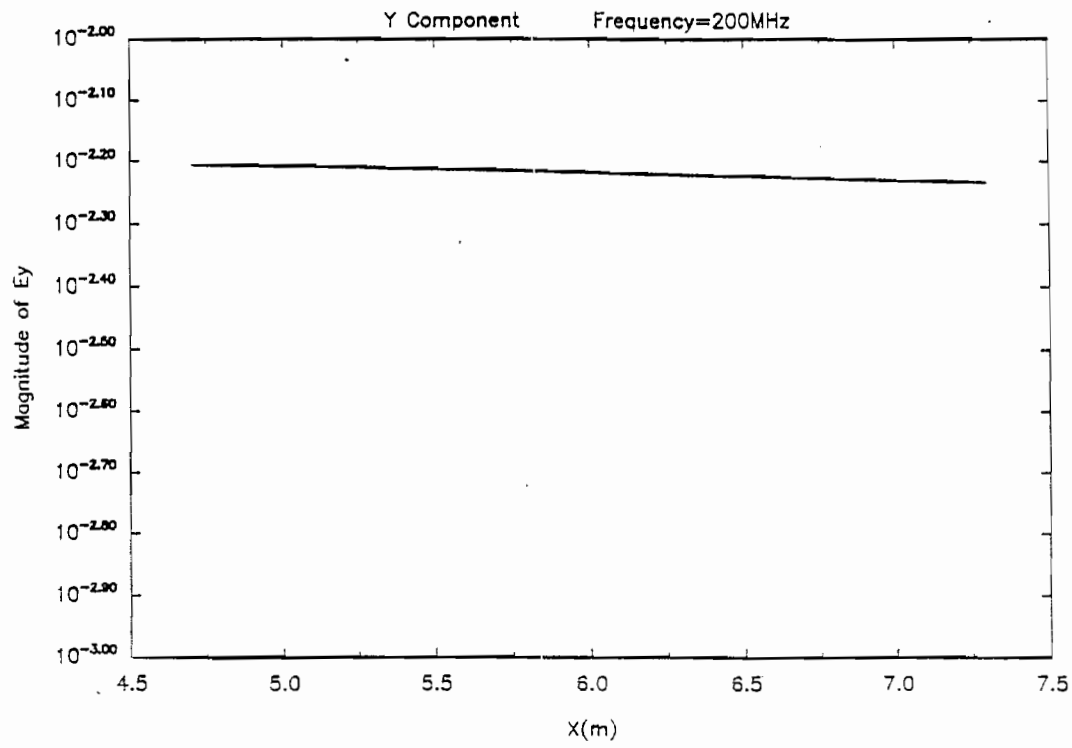


Figure 4-18: Incident E Field along Line $y=0m$ and $z=0m$

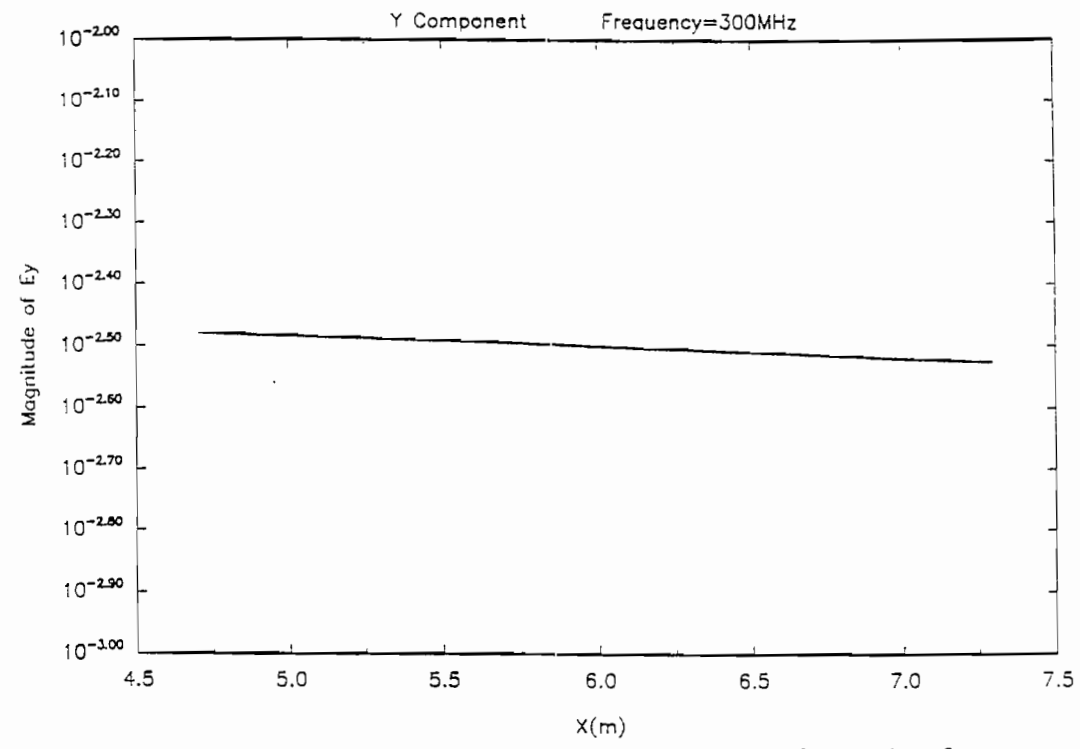


Figure 4-19: Incident E Field along Line $y=0m$ and $z=0m$

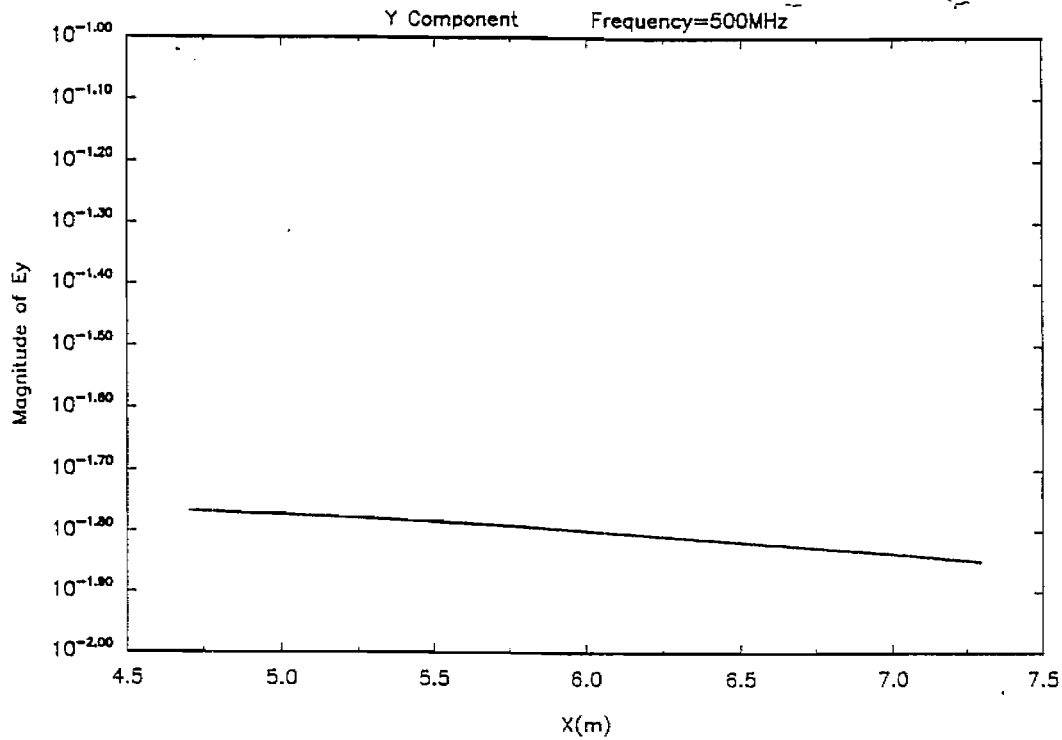


Figure 4-20: Incident E Field along Line $y=0m$ and $z=0m$

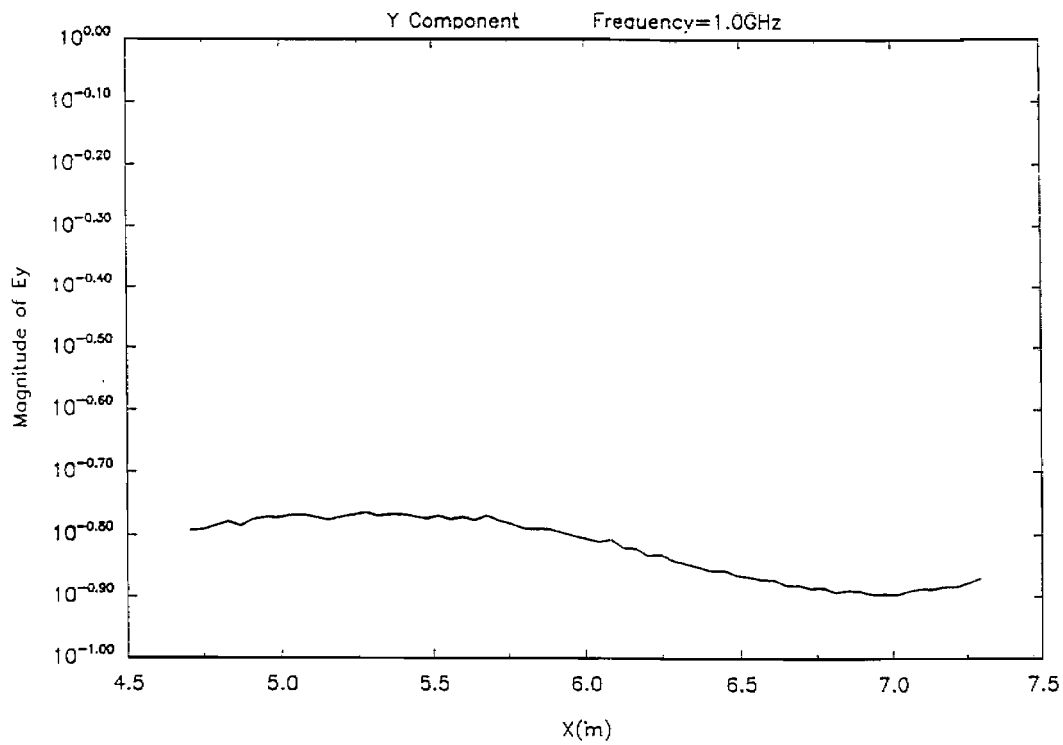


Figure 4-21: Incident E Field along Line $y=0m$ and $z=0m$

4.2 Measured Antenna Power Patterns

What follows are the results obtained from measuring the antenna power pattern of the exponentially tapered transmission line (ETTL) at frequencies of 300 MHz, 500 MHz, 800 MHz, and 1 GHz. The dimensions and construction of the ETTL are detailed in section 3-6.

The apparatus used to measure the power pattern of the ETTL at each of the four frequencies consist mainly of two half-wave dipoles cut for the specific frequency in use, a signal source with external 1000 Hz sinusoidal modulation to drive the transmitting dipole, a detection circuit to receive the signal with either the dipole or the ETTL, and a pattern plotter. The basic apparatus is illustrated in Figure 4-22 below. Here, antenna (1) is a reference dipole and antenna (2) is the ETTL.

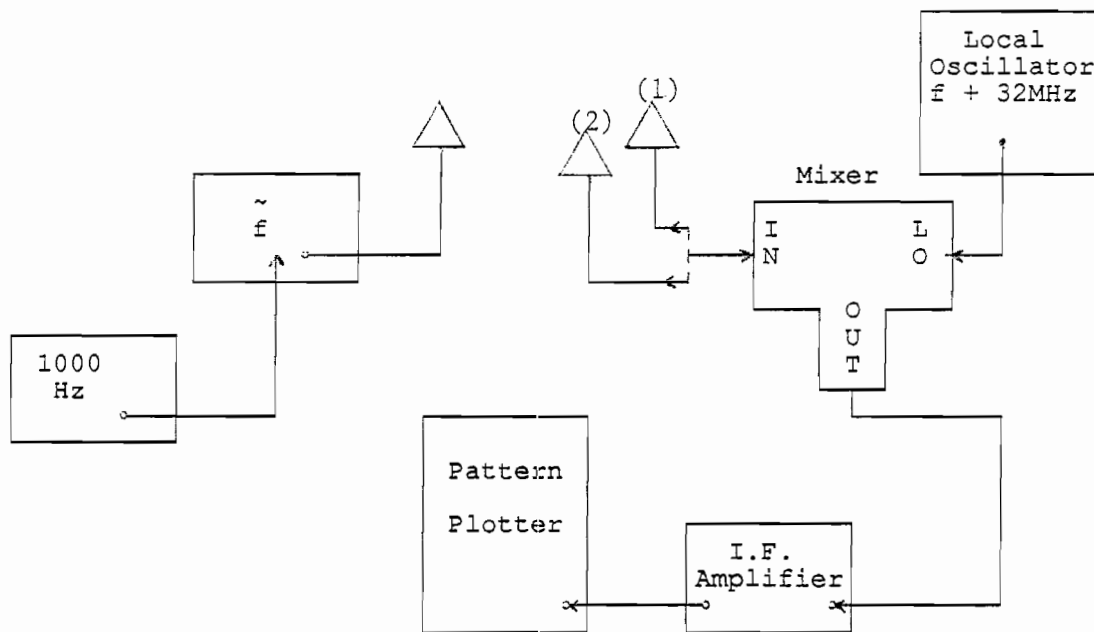


Figure 4-22: Block Diagram of the Pattern Plotting Apparatus

Photographs of the apparatus as it is being used are presented in Figures 4-23 through 4-29 below.

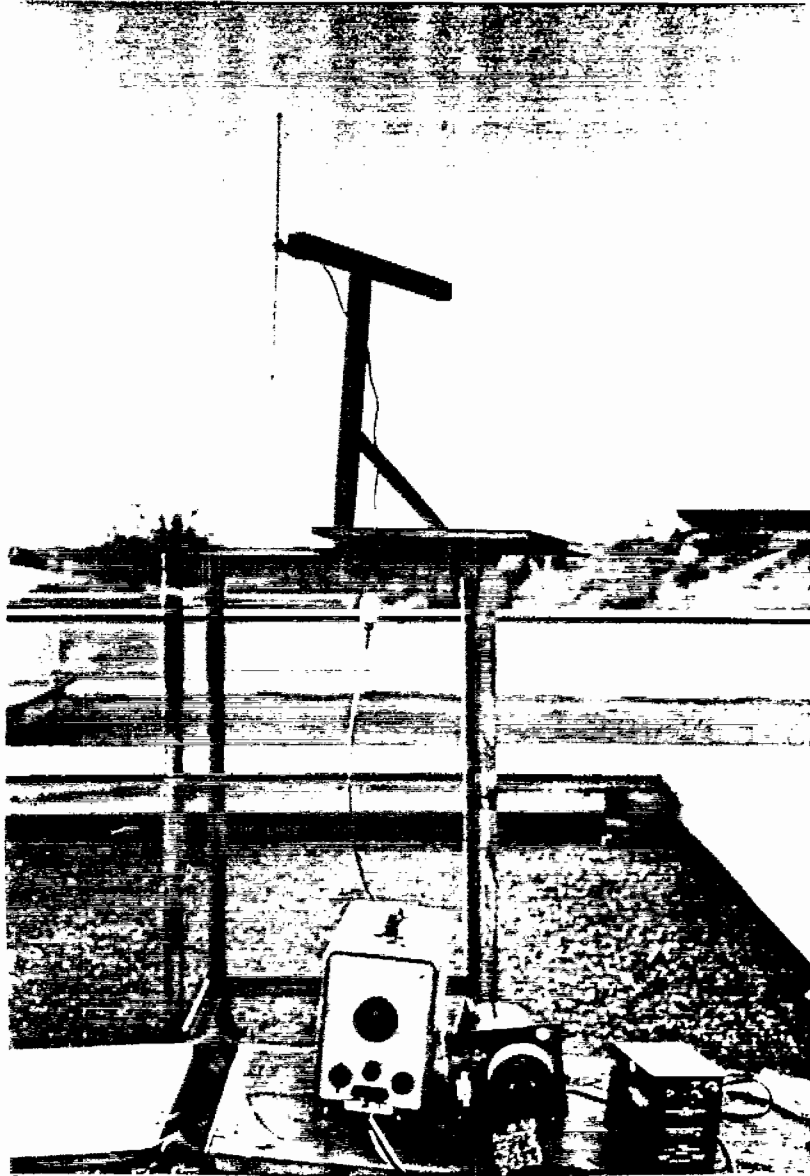


Figure 4-23: Transmitting Half-Wave Dipole Antenna and its Signal Source with 1000 Hz External Modulation. Frequency in Use Is 300 MHz.

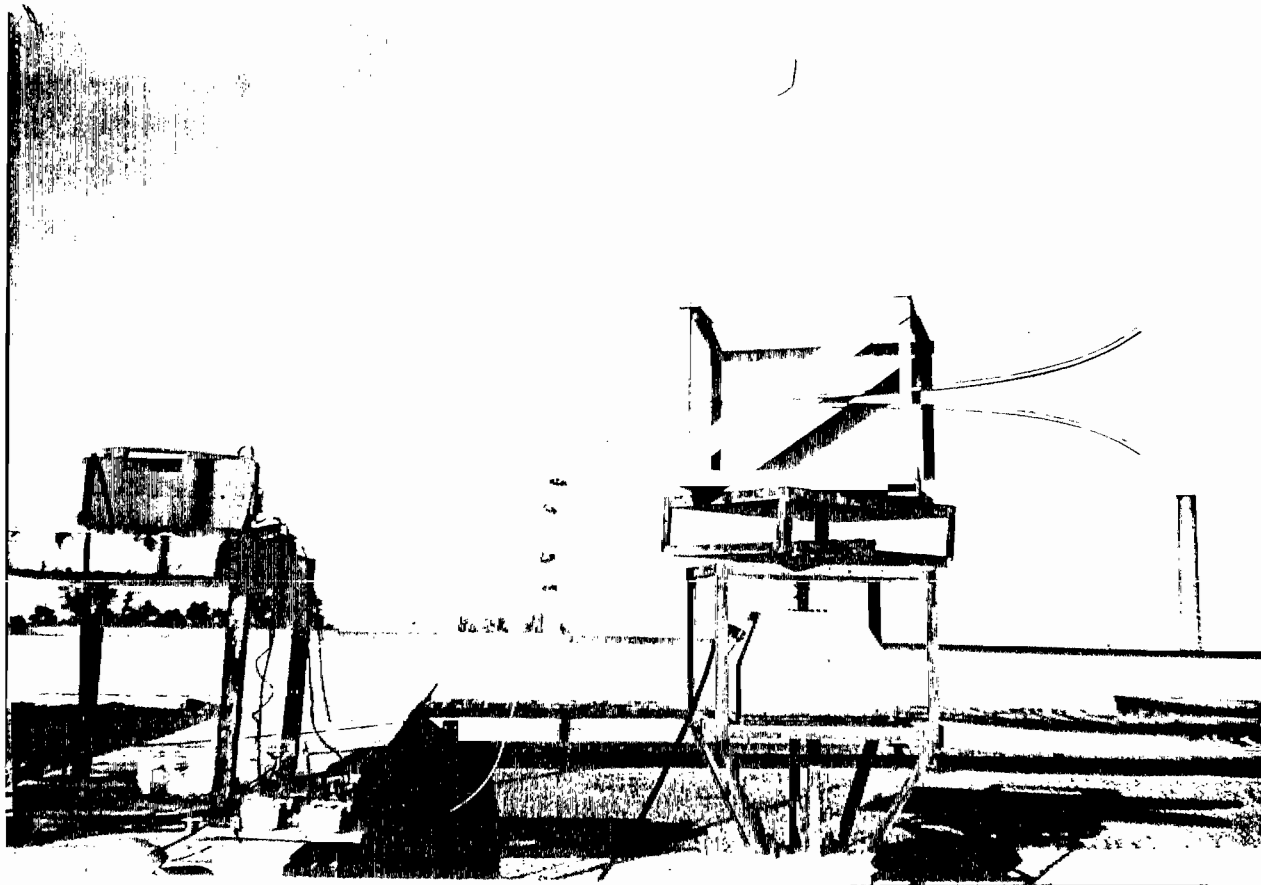


Figure 4-24: E TTL on Pattern Plotter Turntable, Received Signal Is Being Input to the Detection Circuit at the Left.

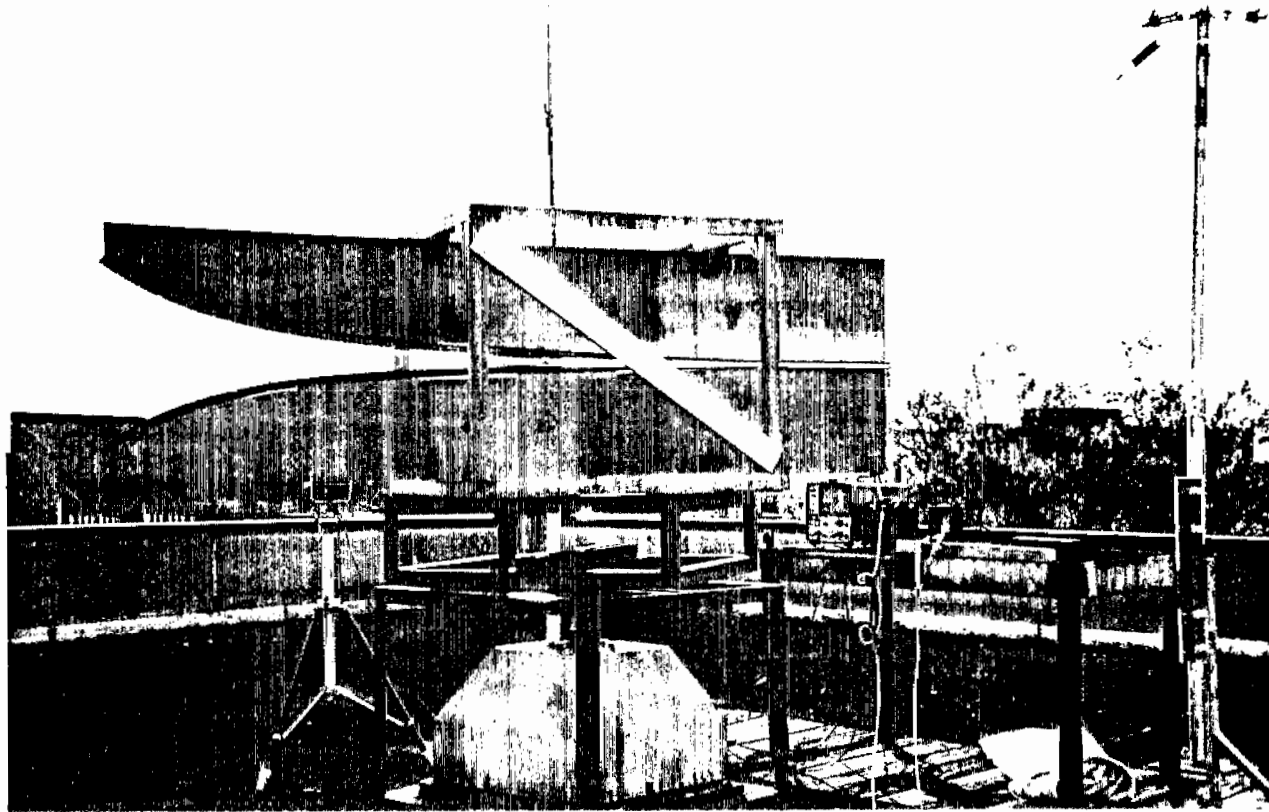


Figure 4-25: Another Angle of Figure 4-24.

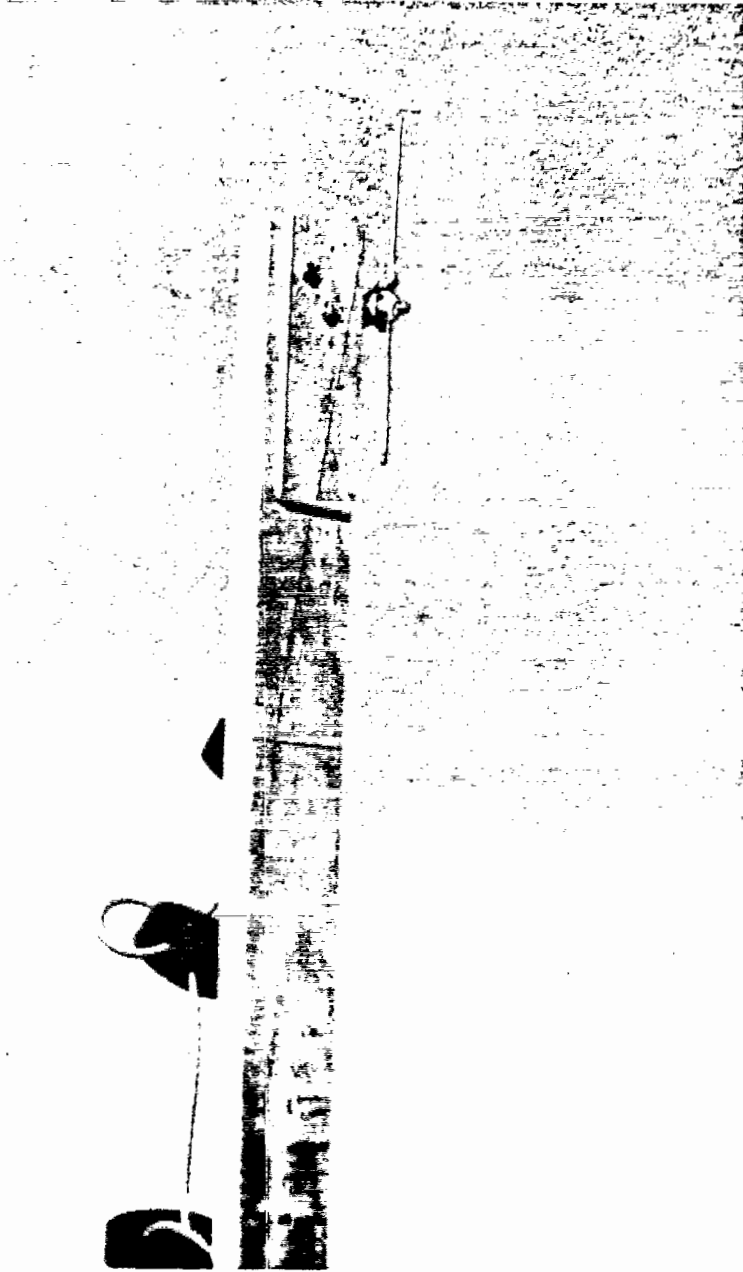


Figure 4-26: Half-Wave Dipole Receiving at 1.0 GHz.
Ferrite Cores Were Used to Reduce Reflections
from the Coaxial Feedline.

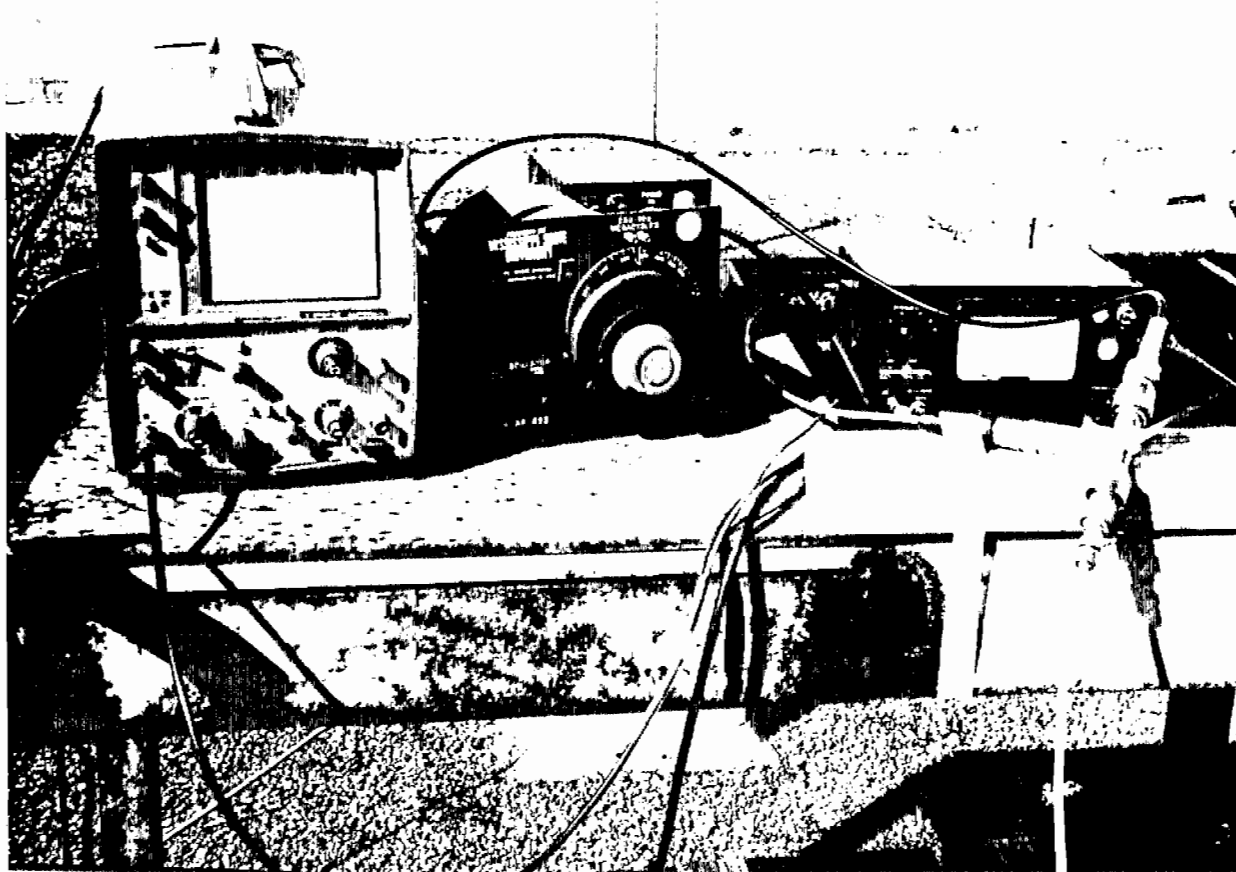


Figure 4-27: Detection Circuit Used to Detect the Received Signal. The Output of the IF Amplifier Is Being Observed on an Oscillator for a Maximum Received Signal Strength. Once Tuned, This Signal Is Sent to the Pattern Plotter.

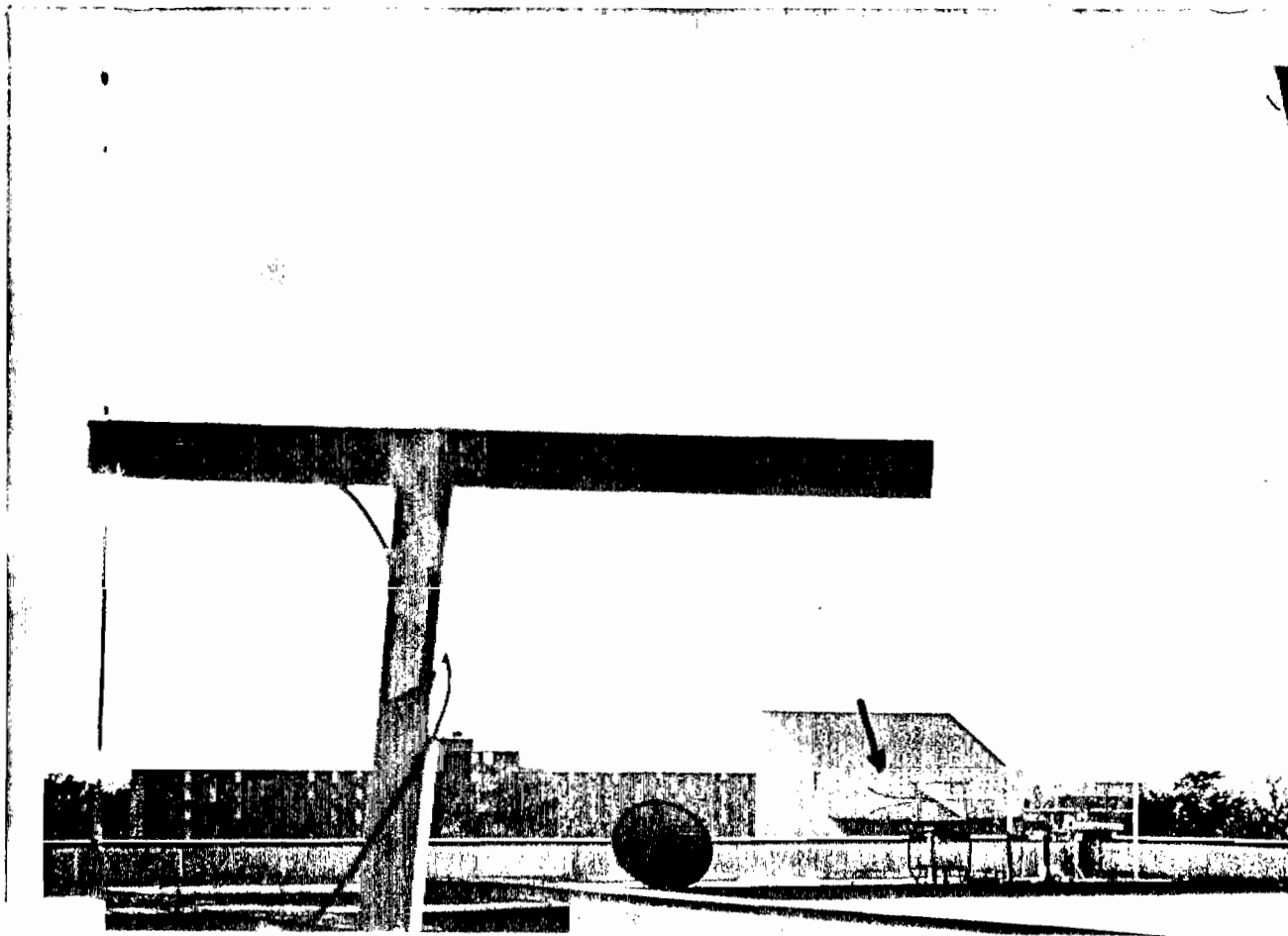


Figure 4-28: Half-Wave Dipole in Foreground at the Left Is Transmitting at 300 MHz. The ETTL in the Distant Background (Indicated with an Arrow) Is Receiving the Signal on the Turntable of the Pattern Plotter.

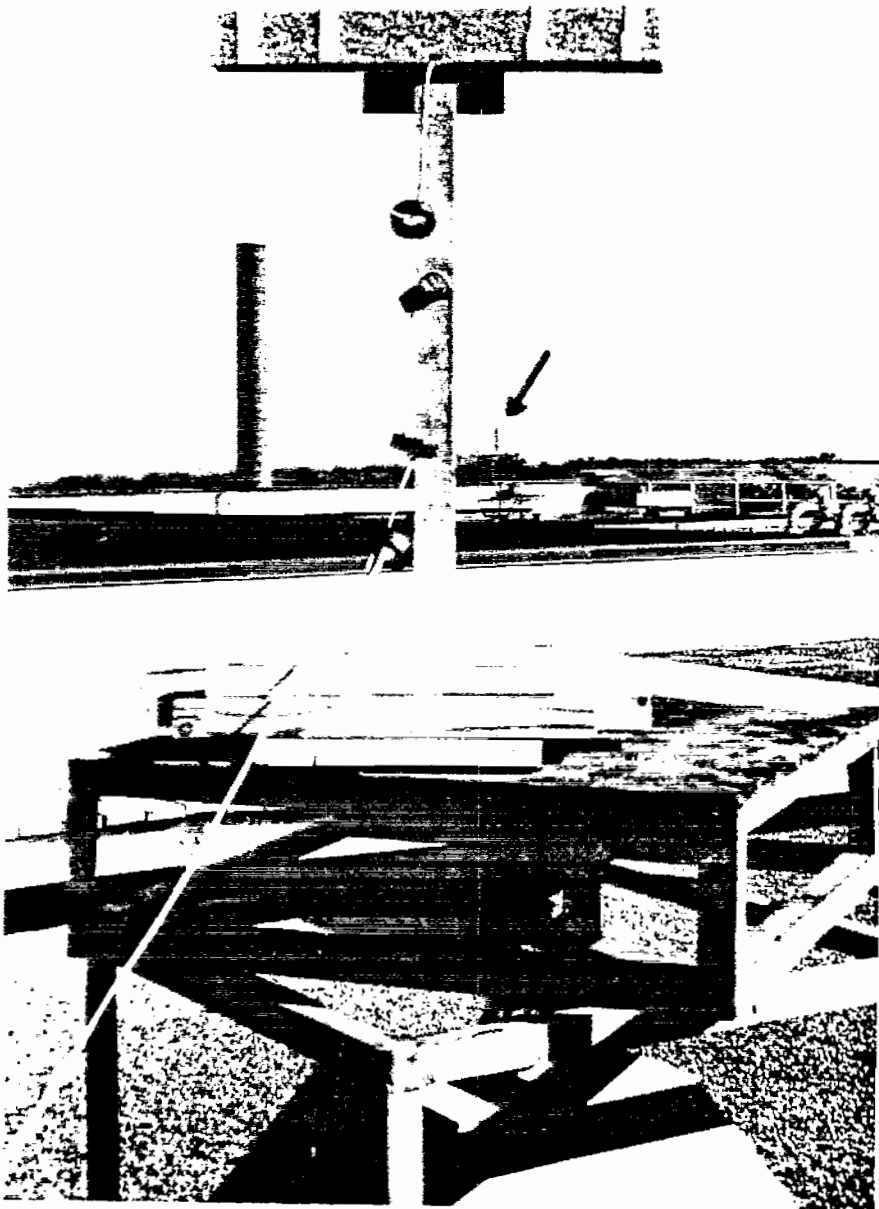


Figure 4-29: Half-Wave Dipole on the Plotter Turntable Receiving a Signal at 300 MHz from the Transmitting Dipole in the Background (Indicated with an Arrow).

At each of the test frequencies, the power pattern for a half-wave dipole is superimposed over that of the ETTL for 3 different configurations: (1) horizontal polarization, (2) horizontal polarization with a large wire loop connected to the ETTL, and (3) vertical polarization. The resulting plots follow in Figures 4-30 through 4-41. The large wire loop used in the second horizontally polarized test consists simply of an approximately 40 ft length of 10 gauge solid copper wire connected across the output terminals of the ETTL in the shape of a large semicircle.

The resulting antenna power patterns yield very similar results for the 500 MHz, 800 MHz, and 1 GHz cases. In each of these cases the horizontal polarization tests, both with and without the large wire loop, yield half-power beamwidths of 34 to 35 degrees. The vertical polarization tests yield half-power beamwidths of 42 degrees and 45 degrees in each of these three cases. The 300 MHz case yields no measurable half-power beamwidth when horizontally polarized due to its nearly constant gain, but when vertically polarized it yields a 64 degree half-power beamwidth.

In the antenna power pattern plots that follow, the horizontal scaling is in 3 degree steps and the smallest vertical divisions are 0.2 dB each.

Some similarities between the incident electric plots and the antenna power pattern plots can be noted. The angles to the first null along line a of Figure 4-1 at 500 MHz and 1 GHz (see Figures 4-10 and 4-11) are approximately 26.6 degrees and 33 degrees respectively, both of which match closely their corresponding antenna power pattern plots. The half-power beamwidth along line a of Figure 4-1 at 1 GHz is approximately 36 degrees, which again is close to that measured for the ETTL. Along line b of Figure 4-1 at 300 MHz and 500 MHz (see Figures 4-19 and 4-20), the half-power beamwidths are 55.1 degrees and 41.3 degrees respectively. These also fall reasonably close to the measured values for the ETTL.

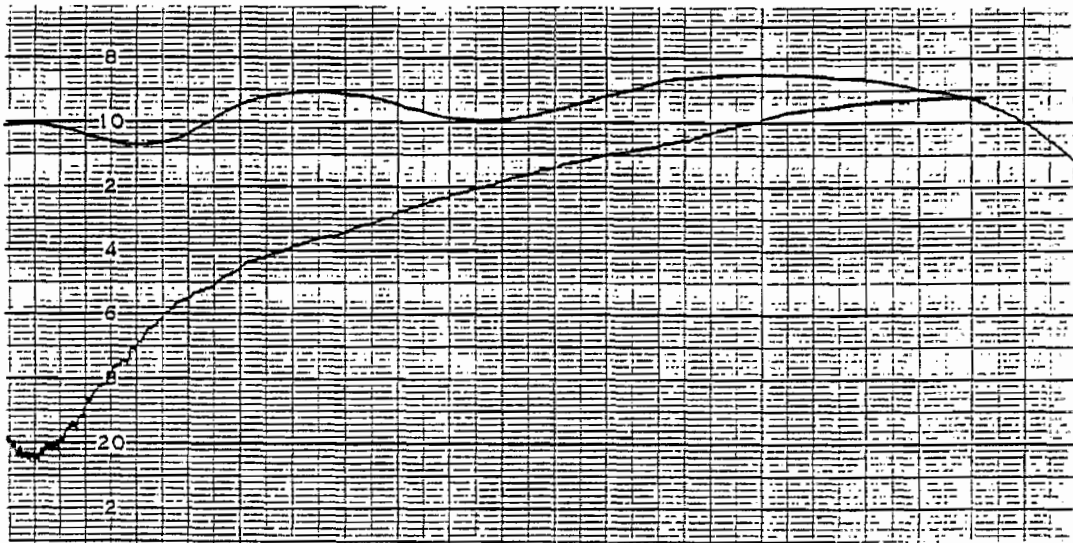


Figure 4-30: Antenna Power Pattern of the ETTL and a Half-Wave Dipole at 300 MHz with Horizontal Polarization.

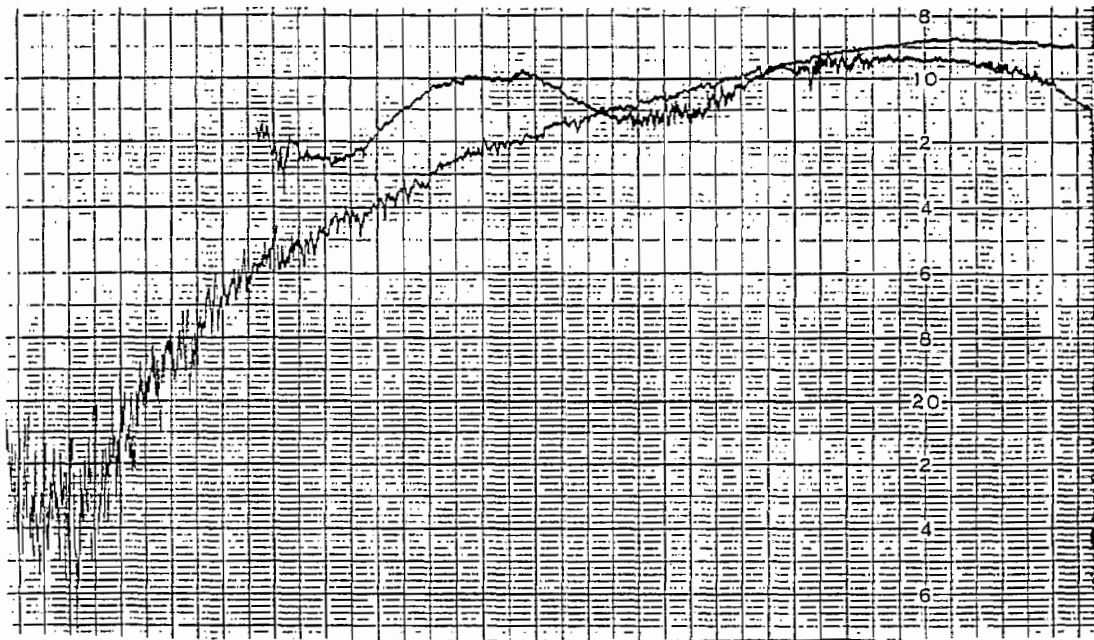


Figure 4-31: Antenna Power Pattern of the ETTL and a Half-Wave Dipole at 300 MHz with Horizontal Polarization and a Large Wire Loop Connected to the ETTL.

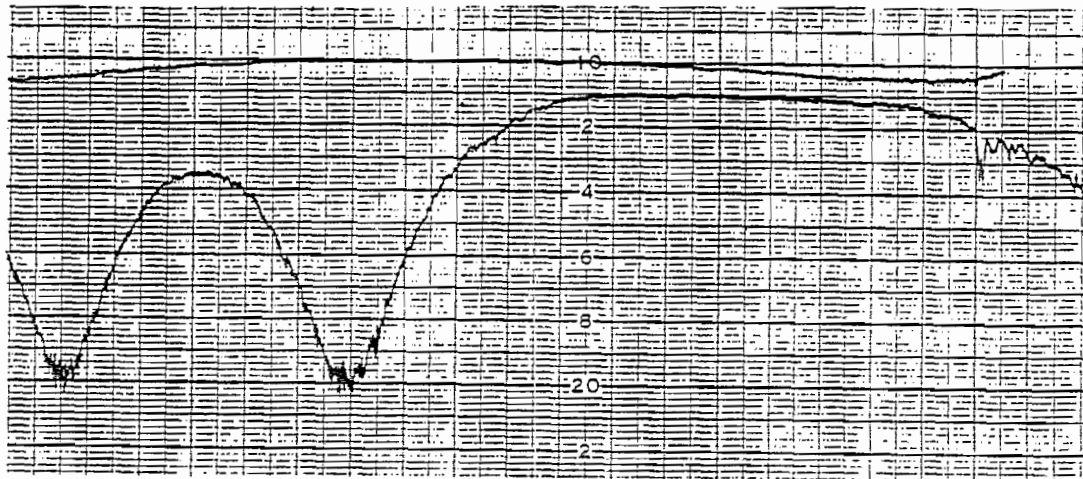


Figure 4-32: Antenna Power Pattern of the ETTL and a Half-Wave Dipole at 300 MHz with Vertical Polarization.

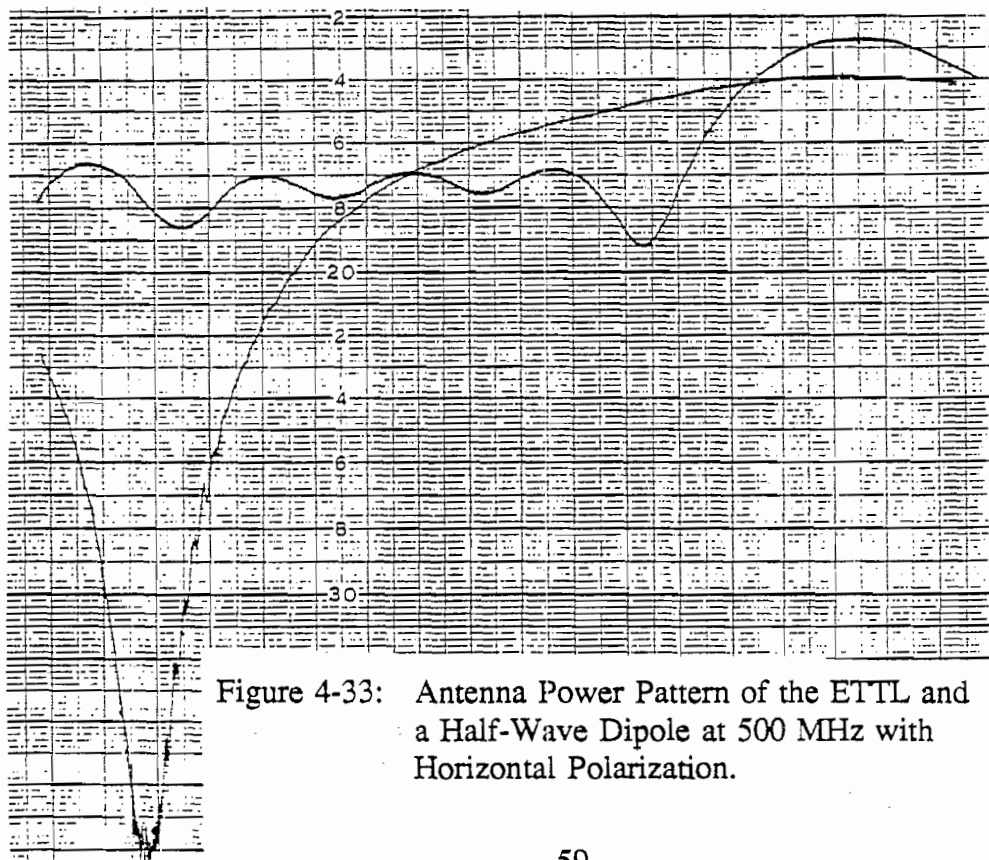


Figure 4-33: Antenna Power Pattern of the ETTL and a Half-Wave Dipole at 500 MHz with Horizontal Polarization.

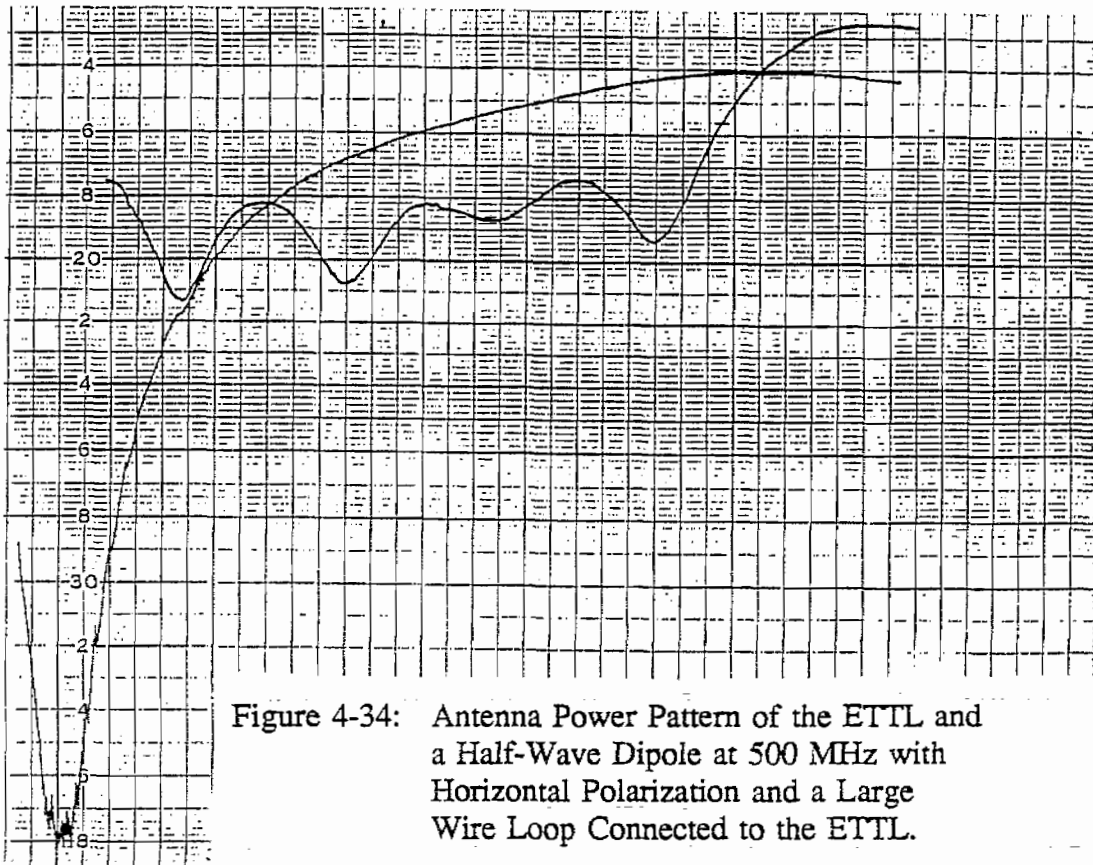


Figure 4-34: Antenna Power Pattern of the ETTL and a Half-Wave Dipole at 500 MHz with Horizontal Polarization and a Large Wire Loop Connected to the ETTL.

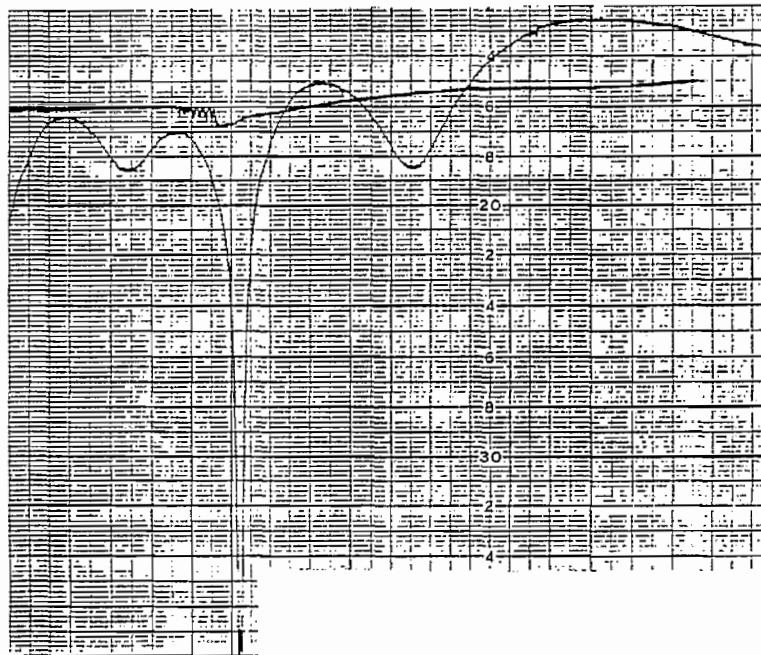


Figure 4-35: Antenna Power Pattern of the ETTL and a Half-Wave Dipole at 500 MHz with Vertical Polarization.

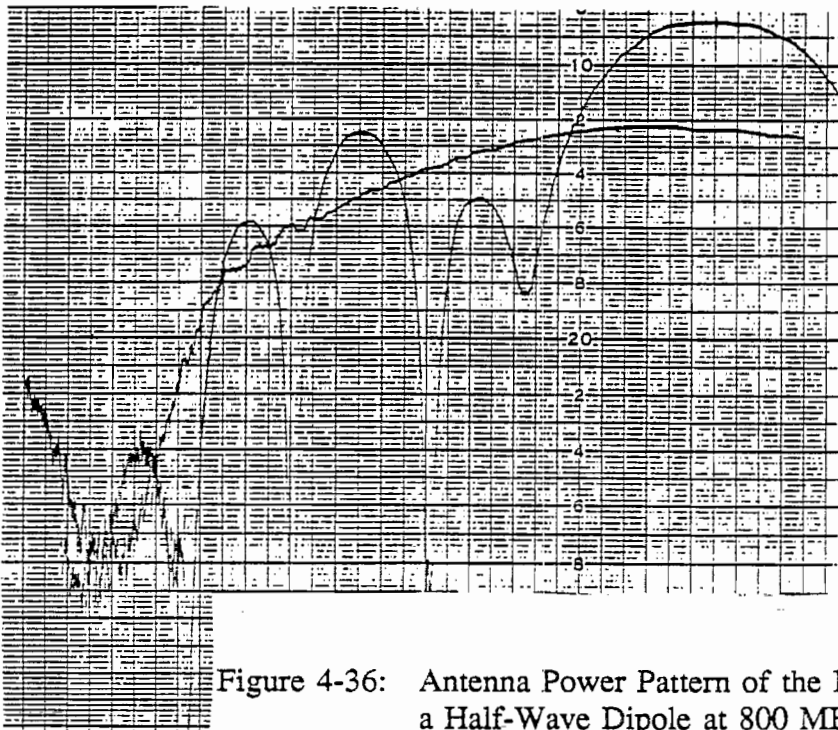


Figure 4-36: Antenna Power Pattern of the ETTL and a Half-Wave Dipole at 800 MHz with Horizontal Polarization.

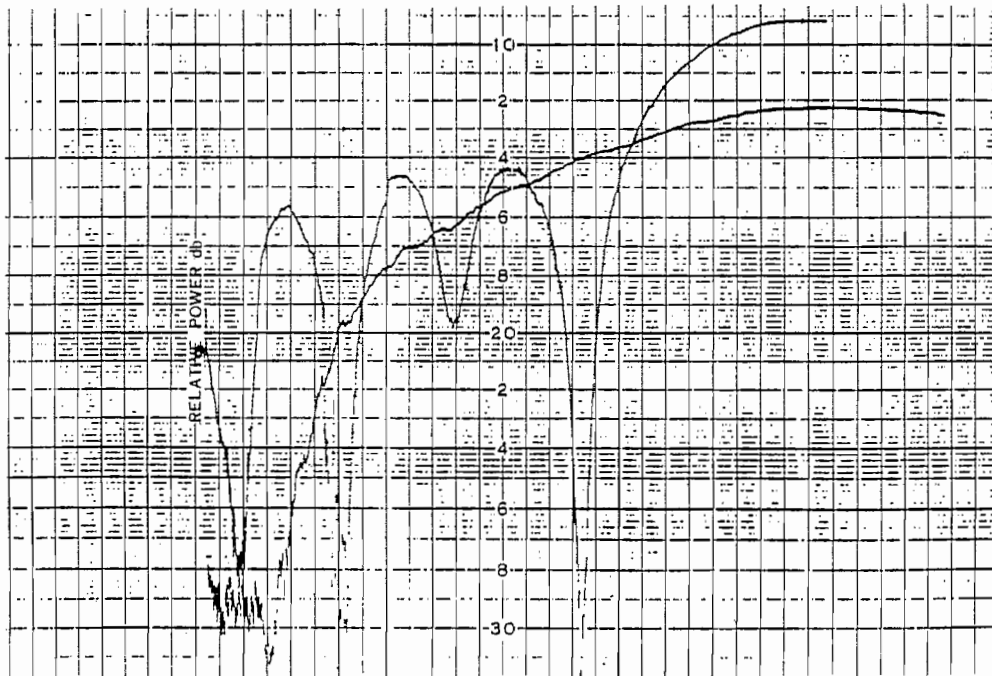


Figure 4-37: Antenna Power Pattern of the ETTL and a Half-Wave Dipole at 800 MHz with Horizontal Polarization and a Large Wire Loop Connected to the ETTL.

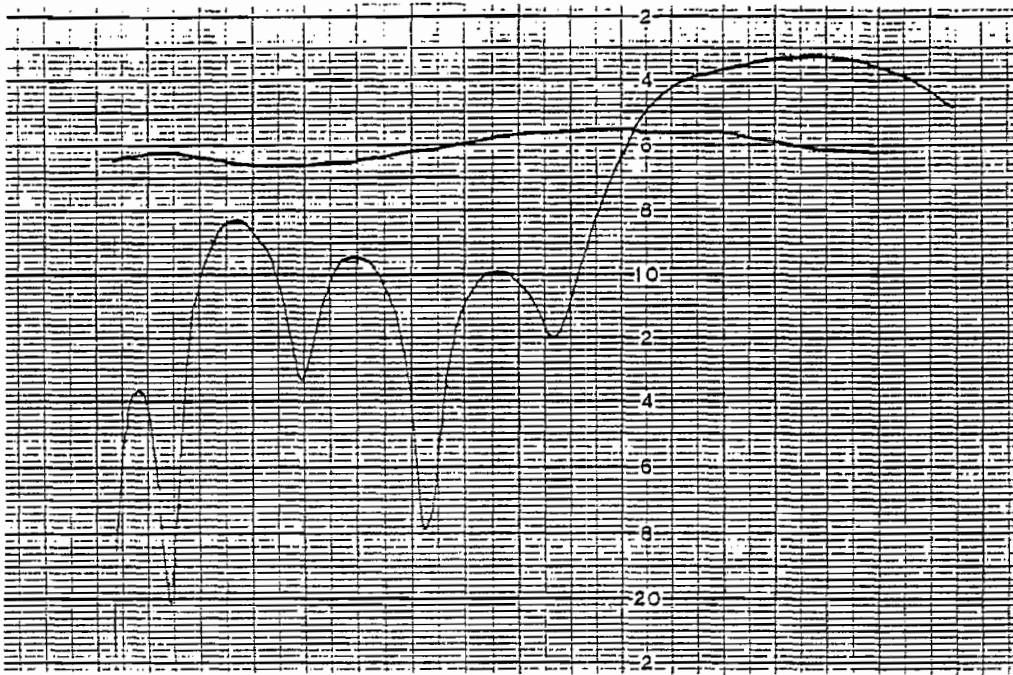


Figure 4-38: Antenna Power Pattern of the ETTL and a Half-Wave Dipole at 800 MHz with Vertical Polarization.

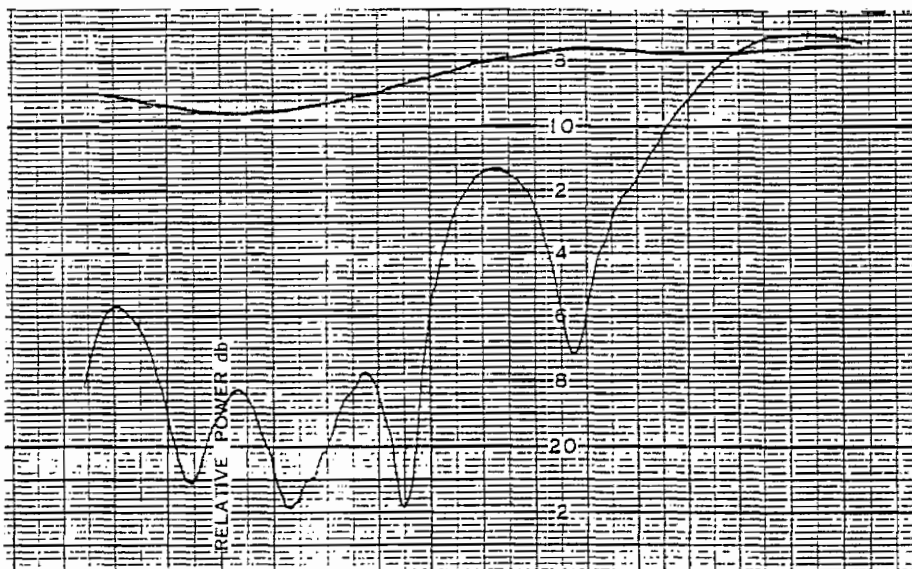


Figure 4-39: Antenna Power Pattern of the ETTL and a Half-Wave Dipole at 1 GHz with Horizontal Polarization.

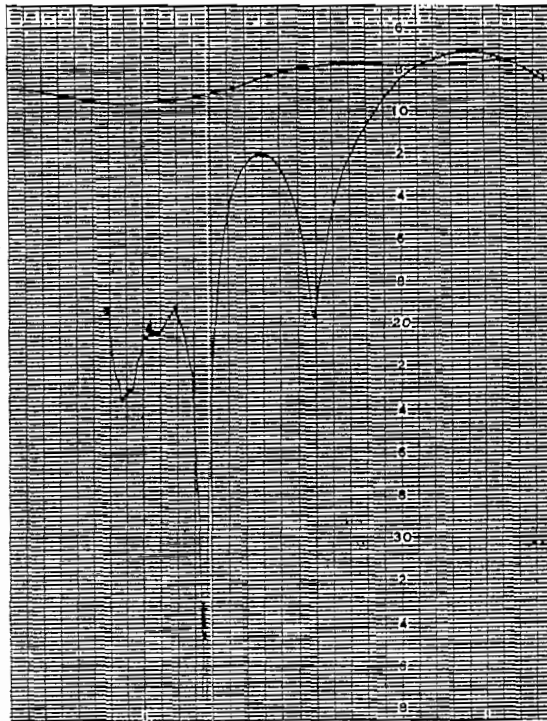


Figure 4-40: Antenna Power Pattern of the ETTL and a Half-Wave Dipole at 1 GHz with Horizontal Polarization and a Large Wire Loop Connected to the ETTL.

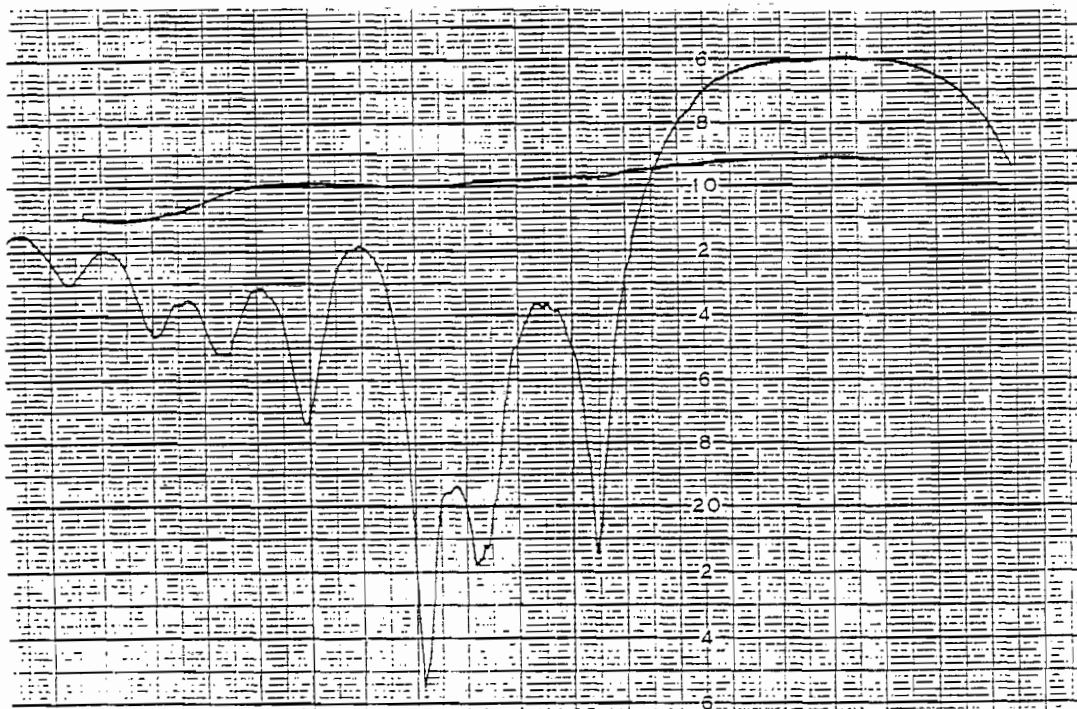


Figure 4-41: Antenna Power Pattern of the ETTL and a Half-Wave Dipole at 1 GHz with Vertical Polarization.

4.3 Input Impedance Calculation

The input impedance for the ETTL is derived earlier in section 3-1 and the method for using the results of the NEC-2 modeling to compute the input impedance for the EI is described. The resulting computed input impedances of the EI are tabulated in Table 4-3 below.

Table 4-3 Calculated input impedances of the EI
 using results obtained from the NEC-2
 modeling at various frequencies.

<u>FREQUENCY (MHz)</u>	<u>INPUT IMPEDANCE (OHMS)</u>	<u>VSWR</u>
0.1	1854.6 - j 50.5	37.1
0.2	1834.9 - j 132.3	36.9
0.3	1894.0 - j 257.3	38.0
0.4	1873.3 - j 415.2	39.3
0.5	1846.6 - j 635.4	41.3
0.6	1778.2 - j 820.2	43.1
0.7	1628.9 - j 994.4	44.7
0.8	1426.1 - j 1125.4	46.3
0.9	1230.1 - j 1209.4	48.4
1.0	1014.8 - j 1188.2	48.1
5.0	203.8 - j 364.3	17.3
10.0	78.6 - j 236.7	16.4
100.0	10.8 - j 1.3	4.6
200.0	82.4 + j 161.4	6.6
300.0	20.1 + j 18.6	2.9
500.0	13.6 - j 11.7	3.9
1000.0	56.8 - j 75.9	3.8

4.4 Input Impedance Measurement

Results of measuring the S parameters of the ETTL with a network analyzer and computing the corresponding input impedances are presented in this section. The ETTL is tested inside a laboratory room in two different positions within the

room. Also, a large wire, no. 12 A.W.G., loop (about 4m in diameter), is placed as a load on the output terminals of the ETTL (as is done in the antenna pattern measurements of section 4-2) in one of the two positions. The different positions are used to try to gauge the affects of the test being conducted indoors in close proximity to possible sources of perturbation. The wire loop is used in one case to observe possible affects of connecting the ETTL to the EI structure as a transition section.

Of the four S parameters measured, S_{11} alone is used to compute the input impedance of the ETTL. These measurements are made from 100 MHz to 1 GHz in 50 MHz steps. The resulting values of Z_{in} are tabulated in Table 4-4 below. Apparently, the connection to the wire loop provides only a small perturbation in the input impedance measurement. Moreover, it appears that the input impedance at high frequency is near the design goal of 50Ω .

Photographs of the testing apparatus are presented in Figures 4-42 and 4-43 respectively.

4.5 Current Computation

The output data of the NEC modeling of the EI also contains the computed currents on the structure. By observing the magnitude of these currents at different frequencies, the portions of the structure that are contributing most strongly to the radiated fields can be seen.

Plots of the magnitude of these currents from NEC models at 200 MHz up to 1 GHz are presented in Figures 4-44 through 4-47. On each plot, the junction of the main EI structure with the transition section is indicated. Note that the wire current amplitude decreases rapidly with distance from the driving point at high frequency.

Table 4-4 Measured input impedances of the ETTL
 A: in one position within the lab room
 B: in same position with large wire loop added
 C: in a second position within the lab room

<u>FREQUENCY</u> <u>(MHz)</u>	<u>INPUT IMPEDANCE</u> <u>FOR TEST A</u>	<u>INPUT IMPEDANCE</u> <u>FOR TEST B</u>	<u>INPUT IMPEDANCE</u> <u>FOR TEST C</u>
100	29.89 - j 12.01	60.50 + j 3.09	30.07 - j 11.76
150	156.04 + j 163.58	74.82 + j 0.92	153.85 + j 173.23
200	84.34 - j 45.31	75.36 - j 7.22	84.94 - j 45.75
250	15.96 + j 4.96	63.08 + j 0.96	15.16 + j 5.22
300	107.29 + j 52.30	112.07 + j 11.99	101.81 + j 48.12
350	232.07 - j 45.83	98.66 - j 3.29	236.44 - j 69.42
400	29.08 + j 2.96	51.40 + j 0.22	30.79 + j 2.72
450	40.14 - j 5.10	47.37 - j 1.04	39.95 - j 5.07
500	105.57 - j 20.79	66.27 - j 5.29	104.40 - j 22.35
550	52.85 - j 1.43	52.92 - j 0.64	52.17 - j 1.14
600	44.68 - j 0.91	66.33 + j 1.53	41.81 - j 1.14
650	134.60 + j 20.85	110.72 + j 2.05	138.56 + j 22.33
700	72.64 - j 6.14	60.86 - j 0.29	70.08 - j 4.91
750	39.41 - j 1.01	52.64 + j 0.42	39.01 - j 0.98
800	50.10 + j 0.02	50.50 + j 0.07	49.13 - j 0.21
850	80.73 - j 8.31	70.05 - j 3.88	80.80 - j 8.11
900	29.62 + j 0.23	34.40 - j 0.76	28.80 + j 0.20
950	70.48 + j 0.39	78.02 - j 0.94	68.19 + j 0.56
1000	70.48 + j 0.39	78.02 - j 0.94	68.19 + j 0.56

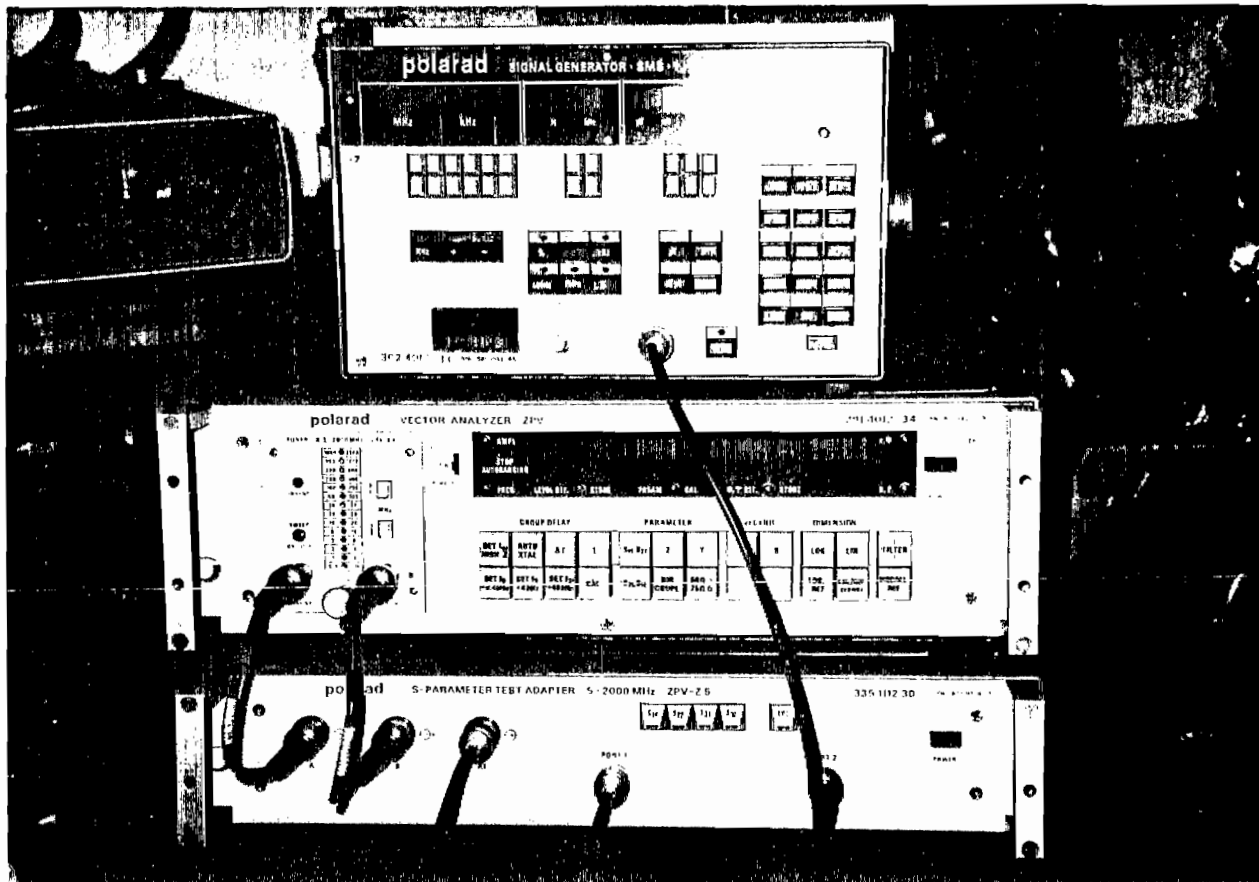
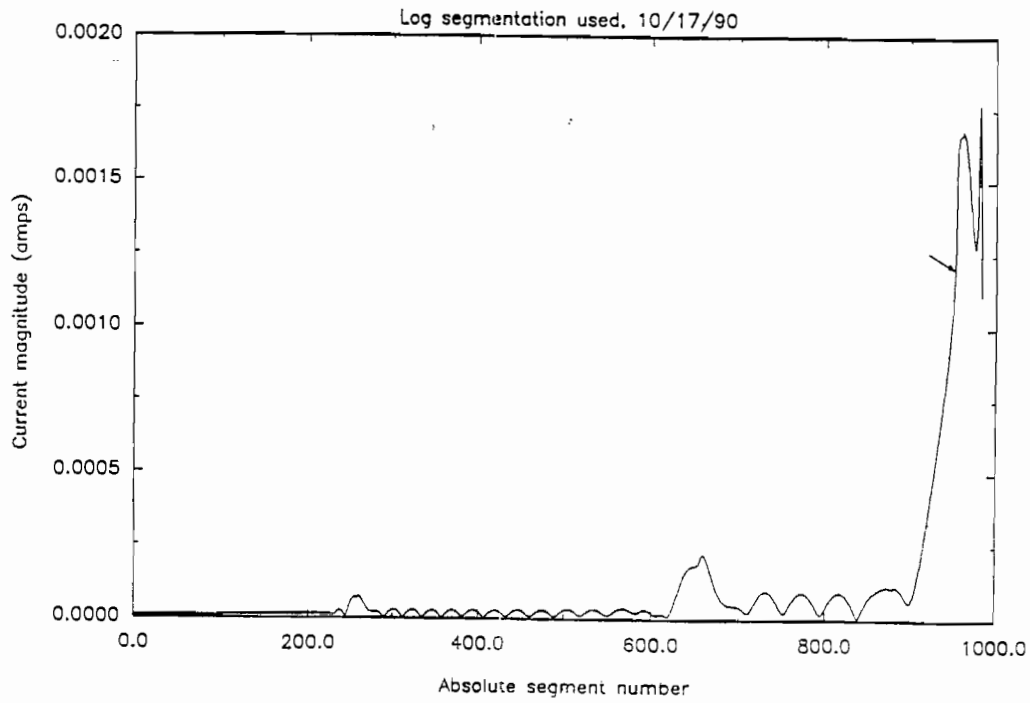


Figure 4-42: Network Analyzer Used to Measure the S Parameters of the ETTL.

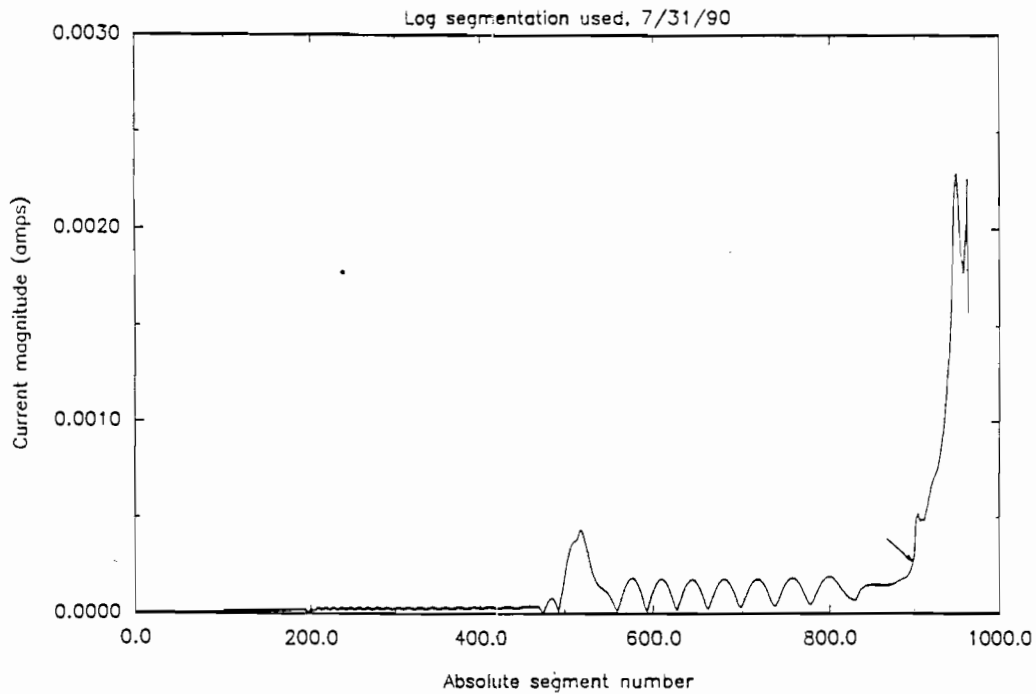


Figure 4-43: Measuring the S Parameters of the E TTL. (This Particular Position Is not Presented in Table 4-2).



(Note: Transition section falls right of the arrow)

Figure 4-44: Current on 1/2 Structure at 200 MHZ



(Note: Transition section falls right of the arrow)

Figure 4-45: Current on 1/2 Structure at 300 MHZ

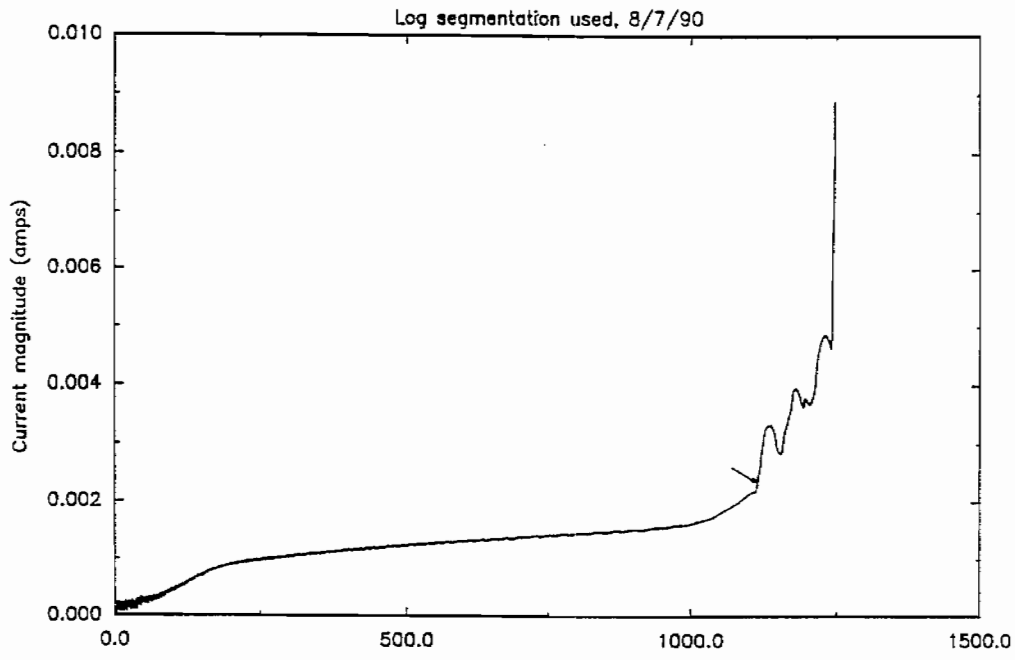


Figure 4-46: Current on 1/2 Structure at 500 MHz

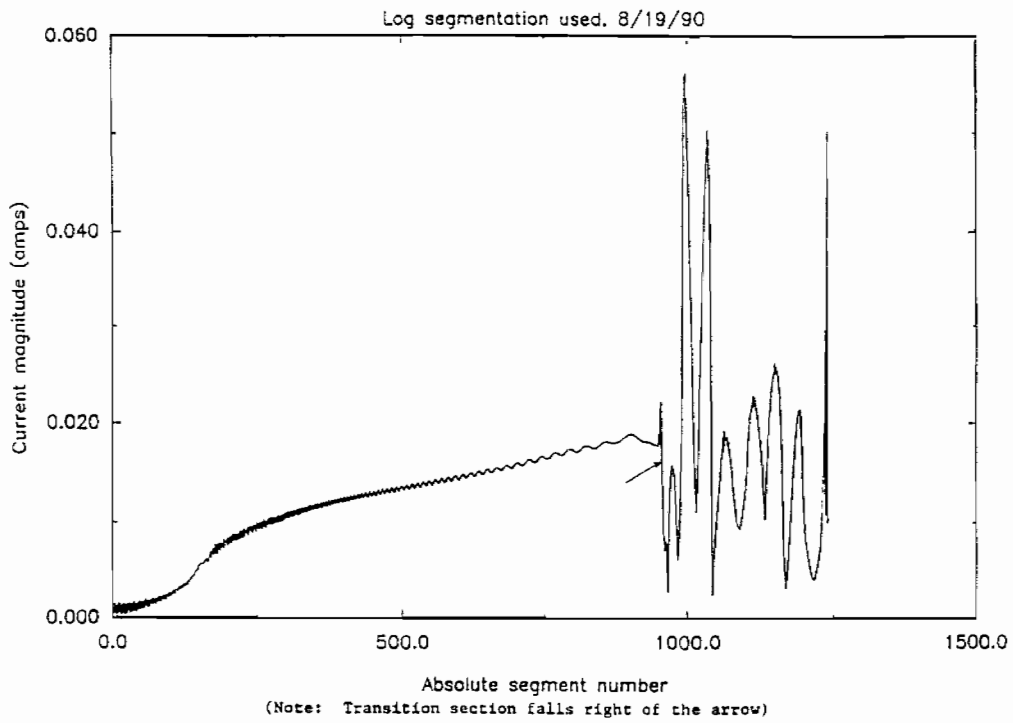


Figure 4-47: Current on 1/2 Structure at 1 GHz

V Conclusion

Numerical techniques have been utilized to examine the electromagnetic fields that can be developed in the working volume of the CW Ellipticus antenna operated at frequencies ranging from approximately 100 KHz to 1 GHz with an exponentially tapered input section. The NEC code is used to analyze the Ellipticus configuration with the transition section present. The input transition section is needed for impedance matching and to drive efficiently the Ellipticus antenna.

A prototype of the input transition section was designed, constructed, and tested at Mississippi State University. The calculated design is verified by measurements done within the antenna pattern range and by impedance measurements. Calculations from the NEC code indicate that field uniformity is achieved within the working volume of the Ellipticus antenna.

References

1. W.D. Prather and C.E. Baum, "Elliptic CW Antenna Design," Miscellaneous Simulator Memos, Memo 22, 16 March 1987.
2. C. Zuffada, F.C. Yang, and I. Wong, "On the Thin Toroidal and Elliptical Antennas," Sensor and Simulation Notes, Note 315, January 1989.
3. G.J. Burke and A.J. Poggio, "Numerical Electromagnetics Code (NEC) Method of Moments," Naval Ocean Systems Center Technical Report NOSCTSD 116, Jan. 1981.
4. J.P. Donohoe and S.N. Tabet, "HSI High Frequency Performance Verification/Upgrade," Final Report Contract No. F29601-88-C-0001, Subtask 03-05/00, November 15, 1989.
5. Tom Dana, "Elliptic CW Antenna System as built Drawings," U.I.E. Technical Report TR-89-0026, December 1989.
6. V. Kamachandran and K.K. Nair, "Equivalent Circuits of an Exponential Transmission Line," IRE Transactions on Circuit Theory, Vol. CT-7, No. 1, pp 71-74, March 1960.
7. John D. Kraus, Electromagnetics, 3rd ed., McGraw-Hill, Inc., New York, 1984, p 401.
8. C.W. Harrison, Jr., "Folded Wire Structures as Receiving Antennas," Technical Memorandum SCTM 253-58-(14), Sandia Corporation, June, 1958.
9. J.P. Castillo and B.K. Singaraju, "Effects of Wave Reflection on Objects Near a Plane Ground," Athamas Memos, memo 8, May 1, 1975.
10. Saad N. Tabet, "High Frequency Performance of the Rhombic Illuminator," Mississippi State University, 1989.
11. R.W.P. King, Transmission Line Theory, Dover Publications, New York, 1965, p 30.
12. Ibid, pp 45-47.
13. R.W.P. King and C.W. Harrison, Jr., "Current Distribution and Impedance Per Unit Length of Thin Strip," IEEE Transactions on Antennas and Propagation, Vol. AP-14, No. 2, p 252, March 1966.

14. Samuel Seely and Alexander D. Poularikas, Electromagnetics, Marcel Dekker, Inc., New York, 1979, pp 73-90.
15. William H. Hayt, Jr., Engineering Electromagnetics, 4th ed., McGraw-Hill, New York, 1981, p 167.
16. Wolfgang Hilberg, Electrical Characteristics of Transmission Lines, Artech House, Inc., Dedham, 1979, pp 1-2.
17. Everett G. Farr, "Extrapolation of Ground-Alert Mode Data at Hybrid EMP Simulators," Sensor and Simulation Notes, Note 311, The BDM Corporation, July 1988.